Available on CMS information server

CMS NOTE 2003/033

The Compact Muon Solenoid Experiment

CMS Note

Mailing address: CMS CERN, CH-1211 GENEVA 23, Switzerland

10 December 2003

Summary of the CMS Potential for the Higgs Boson Discovery

S. Abdullin[1,a], S. Banerjee[2], L. Bellucci[3], C. Charlot[4], D. Denegri[5,b], M. Dittmar[6], V. Drollinger[7], M.N. Dubinin[8], M. Dzelalija[9], D. Green[10], I. Iashvili[10], V.A. Ilyin[8], R. Kinnunen[11], S. Kunori[1] K. Lassila-Perini[11], S. Lehti[11], K. Mazumdar[2], F. Moortgat[12], Th. Muller[13], A. Nikitenko[14,a], I. Puljak[9], P. Salmi[11], C. Seez[14], S. Slabospitsky[15], N. Stepanov[5,a], R. Vidal[10], W. Wu[10], H.D. Yildiz[16], M. Zeyrek[16]

Abstract

This work summarizes the studies for the Higgs boson searches in CMS at the LHC. The main discovery channels are presented and the potential is given for the discovery of the SM Higgs boson and the Higgs bosons of the MSSM. The phenomenology, detector, trigger and reconstruction issues are briefly discussed.

[1] University of Maryland, College Park, Maryland, U.S.A.

[2] Tata Institute of Fundamental Research, Mumbai, India

[3] Universita di Firenze e Sezione dell'INFN, Firenze, Italia

[4] Ecole Polytechnique, IN2P3-CRNS, Palaiseau, France

[5] European Laboratory for Nuclear Research (CERN)

[6] Eidgenossische Technische Hochschule Zurich/ETH, Zurich, Switzerland

[7] Physics Department of Padua University, Padova, Italy

[8] Institute of Nuclear Physics, Moscow State University, Moscow, Russia

[9] University of Split, Split, Croatia

[10] Fermi National Accelerator Laboratory, Batavia, Illinois, U.S.A.

[11] Helsinki Institute of Physics, Helsinki, Finland

[12] Department of Physics, University of Antwerpen, Antwerpen; Research Assistant FWO-Flanders, Belgium

[13] IEKP, Karlsruhe University, Germany

[14] Imperial College, University of London, London, UK

[15] IHEP, Protvino, Moscow Region, Russia

[16] Middle East Technical University, Ankara, Turkey

[a] On leave from ITEP, Moscow, Russia

[b] DAPNIA/SPP, CE Saclay, Gif-sur-Yvette, France

1 Introduction

The studies for the Higgs bosons searches in CMS are mainly performed in the framework of the Standard Model (SM) and its Minimal Supersymmetric extension (MSSM). In the SM Higgs mechanism, the Higgs boson mass $\mathrm{m_H}$ is the only free parameter. The MSSM contains five Higgs bosons: the lighter scalar h, the heavier scalar H, the pseudoscalar A and the two charged bosons $\mathrm{H^{\pm}}$. At tree level the h(H) mass is bound to be below(above) the Z boson mass but the radiative corrections, proportional to $\mathrm{m_{top}^4}$, bring the upper (lower) bound to a significantly larger value. The one loop and dominant two loop calculations, with the SUSY parameters listed below, predict an upper bound of 127 GeV/c^2 with maximal stop mixing and 113 GeV/c^2 without stop mixing [1]. A general agreement is to present the MSSM parameter space as a function of the pseudoscalar mass $\mathrm{m_A}$ and the ratio tanβ of the vacuum expectation values of the two Higgs boson doublets. For the SUSY parameters, the following values (as used in the LEP studies [2]) are taken unless stated otherwise: $\mathrm{M_2}$ = 200 GeV/c^2, μ = $-$ 200 GeV/c^2, $\mathrm{M_{\tilde{g}}}$ = 800 GeV/c^2, $\mathrm{M_{\tilde{q},\tilde{\ell}}}$ = 1 TeV/c^2. For the no-stop-mixing scenario $\mathrm{A_t}$ is set to zero and for the maximal mixing scenario $\mathrm{A_t}$ is set to 2450 GeV/c^2. The top mass is set to 175 GeV/c^2.

For several years, LEP and the Tevatron have been operating in an energy range allowing the Higgs boson(s) to be directly and indirectly searched for. Although tantalizing hints were observed around 115-116 GeV/c^2, the LEP programme was terminated without conclusive evidence for the Higgs boson. The measurements yield lower bounds of 114.4 GeV/c^2 for the mass of the SM Higgs boson [3] and 91.0 and 91.9 GeV/c^2 for the masses of the h and A bosons in the MSSM [4]. The excluded tanβ regions are 0.5$<$ tanβ $<$ 2.4 for the maximal $\mathrm{m_h}$ scenario and 0.7$<$ tanβ $<$ 10.5 for the no-stop-mixing scenario [4]. The fits to all LEP, SLC and Tevatron precision measurements lead to an indirect prediction for the SM Higgs boson mass of $\mathrm{m_H}$ = 96^{+60}_{-38} GeV/c^2 and to a 95% CL upper limit of 219 GeV/c^2 [5].

This paper summarizes the CMS studies for the SM and MSSM Higgs bosons. In these studies, performed mainly with fast detector simulation, the main detector dependent issues like mass resolutions and efficiencies for reconstruction and b tagging were studied with full simulation and used directly or parametrized in the fast simulation. Studies based solely on the full simulation and complete reconstruction are presently in progress for all the channels with the now frozen detector design. In this paper, the production processes, the decay channels, the search strategy and the influence of the MSSM parameters are discussed in Sections 2.1 to 2.4. The detector is shortly presented in Section 3.1 and the trigger and reconstruction issues are discussed in Sections 3.2 and 3.3. Section 3.4 is devoted to background simulations. The searches for a SM-like scalar Higgs boson are discussed in Section 4.1, those for the neutral Higgs bosons H and A in Section 4.2 and the charged Higgs bosons $\mathrm{H^{\pm}}$ in Section 4.3. Sections 4.4 and 4.5 summarize the discovery potentials in the SM and the MSSM. The specific SUSY searches, the Higgs boson decays to gauginos, the Higgs boson production through gaugino decays and the discovery potential in the specific SUSY searches are discussed in the Sections 5.1 and 5.2. The conclusions are given in Section 6.

2 Phenomenology

2.1 Higgs boson production processes

Figure 1 shows the production cross sections for the SM Higgs boson as a function of the Higgs boson mass for different production processes calculated at QCD leading order with the programs of Ref. [6]. The production is dominated by the gluon-gluon fusion, $\mathrm{gg \to H}$, over the mass range 100 GeV/$c^2 \lesssim \mathrm{m_H} \lesssim$ 1 TeV/c^2. The associated production processes, $\mathrm{qq \to HW}$, $\mathrm{qq \to HZ}$, $\mathrm{gg/qq \to t\bar{t}H}$ and $\mathrm{gg/qq \to b\bar{b}H}$ have cross sections lower by a factor of $\sim$ 20 at $\mathrm{m_H}$ $\sim$ 100 GeV/c^2 and by a factor of $\sim$ 1000 at large masses, $\mathrm{m_H} \gtrsim$ 500 GeV/c^2. The production cross section for the gauge boson fusion, $\mathrm{qq \to qqH}$, is about 10% of the production cross section for $\mathrm{gg \to H}$ for $\mathrm{m_H} \lesssim$ 200 GeV/c^2, and becomes comparable for $\mathrm{m_H} \sim$ 1 TeV/c^2.

In the MSSM, the lighter scalar h is SM-like for $\mathrm{m_A} > \mathrm{m_h^{max}}$ (decoupling region), with production cross sections and decay partial widths close to those of the SM Higgs boson. At large tanβ, the couplings of the heavy neutral Higgs bosons to the electroweak gauge bosons are strongly suppressed, while those to the down-type fermions are enhanced with tanβ. The production of the heavy neutral MSSM Higgs bosons, H and A, proceeds mainly through $\mathrm{gg \to H/A}$ and $\mathrm{gg/qq \to b\bar{b}H/A}$. At large tan$\beta$, the $\mathrm{b\bar{b}H/A}$ associated production dominates and is about 90% of the total rate for tan$\beta \gtrsim$ 10 and $\mathrm{m_A} \gtrsim$ 300 GeV/c^2. The heavy scalar Higgs boson is SM-like near its lower mass bound (i.e. at small $\mathrm{m_A}$ and large tanβ) and has in this region a significant cross section in the gauge boson fusion process $\mathrm{qq \to qqH}$.

If the charged Higgs bosons are light, $\mathrm{m_{H^\pm}} < \mathrm{m_{top}}$, they are predominantly produced in $\mathrm{t\bar{t}}$ events, with a $\mathrm{t \to H^{\pm}b}$

decay. Several processes, like $\mathrm{gb} \to \mathrm{tH}^{\pm}$, $\mathrm{gg} \to \mathrm{tbH}^{\pm}$, $\mathrm{q\bar{q}'} \to \mathrm{H}^{\pm}$, $\mathrm{gg} \to \mathrm{H}^{+}\mathrm{H}^{-}$ and $\mathrm{gg} \to \mathrm{W}^{\pm}\mathrm{H}^{\mp}$ contribute to the production of heavier ($\mathrm{m_{H^{\pm}}} \geq \mathrm{m_t}$) charged Higgs bosons. The cross section for the production in association with one top quark $\mathrm{gb} \to \mathrm{tH}^{\pm}$ is sizeable ($\sim$ 0.1 pb for $\mathrm{m_{H^{\pm}}}$ = 400 GeV/c^2, tanβ = 30) [7]. The direct production, $\mathrm{q\bar{q}} \to \mathrm{H}^{\pm}$, has a cross section comparable to that of $\mathrm{gb} \to \mathrm{tH}^{\pm}$ [8] while for the $\mathrm{gg} \to \mathrm{H}^{+}\mathrm{H}^{-}$ and $\mathrm{gg} \to \mathrm{W}^{\pm}\mathrm{H}^{\mp}$ processes the cross sections are smaller typically by two orders of magnitude [9].

The tan$^2\beta$ dependence of the cross sections of the associated production processes $\mathrm{gg} \to \mathrm{b\bar{b}H/A}$ and $\mathrm{gg} \to \mathrm{btH}^{\pm}$ can be exploited to measure the value of tanβ from the event rates.

The QCD corrections for the $\mathrm{gg} \to \mathrm{H}$ process are large, with a k factor ranging from 1.5 to 1.8 [10]: the next-to-leading (NLO) production cross section for this process is shown in Fig. 1. The QCD corrections are smaller for the gauge boson fusion (k factor $\sim$ 1.1) and for the associated production processes $\mathrm{qq'} \to \mathrm{HW}$, $\mathrm{q\bar{q}} \to \mathrm{HZ}$ (k factor $\sim$ 1.3) and $\mathrm{gg/q\bar{q}} \to \mathrm{t\bar{t}H}$ (k factor $\sim$ 1.2) [10]. For the production of the charged Higgs bosons, the NLO corrections increase the cross section for $\mathrm{gb} \to \mathrm{tH}^{\pm}$ by about 30% [7]. In the next sections the lowest order cross sections are used unless stated otherwise. The scale uncertainties for the associated processes are smaller ($\sim$ 20%) than those for the gluon-gluon fusion process ($\sim$ 60%) [7, 10].

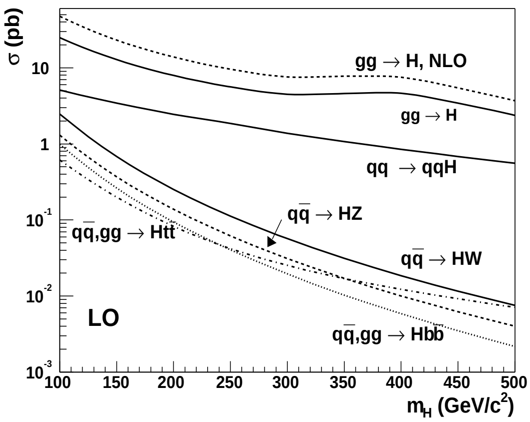

Figure 1: The leading order (LO) cross sections calculated with the programs of Ref. [6] for the SM Higgs boson as a function of $\mathrm{m_H}$. The cross section for the $\mathrm{gg} \to \mathrm{H}$ process is also shown at NLO.

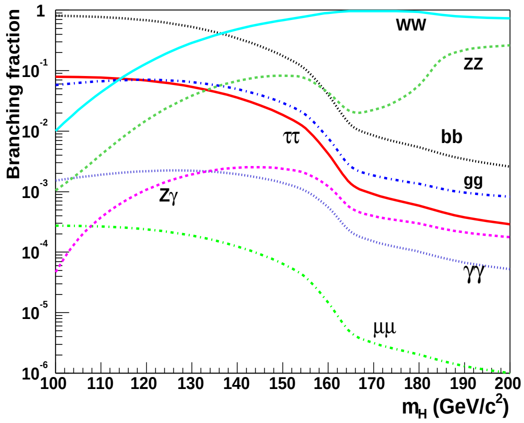

Figure 2: Branching fractions for the SM Higgs boson as a function of $\mathrm{m_H}$ calculated with HDECAY [11].

2.2 Higgs boson decay channels

The branching fractions for the SM-like Higgs boson, calculated with the HDECAY program [11], are shown in Fig. 2 as a function of the Higgs boson mass. For Higgs boson masses below 130 GeV/c^2, the $\mathrm{H} \to \mathrm{b\bar{b}}$ decay channel dominates. In this mass range, the $\mathrm{H} \to \tau^+\tau^-$ decay rate is also sizeable and amounts to $\sim$ 8%. The branching fraction for $\mathrm{H} \to \gamma\gamma$ is about 1.5×10^{-3} for $\mathrm{m_H} \lesssim$ 150 GeV/c^2, that to $\mathrm{H} \to \mu^+\mu^-$ about 2×10^{-4} for $\mathrm{m_H} \lesssim$ 130 GeV/c^2 and the branching fraction to $\mathrm{H} \to \mathrm{Z}\gamma$ about 2×10^{-3} for 140 GeV/$c^2 \lesssim \mathrm{m_H} \lesssim$ 150 GeV/c^2. For larger $\mathrm{m_H}$, the decay is almost entirely through the $\mathrm{H} \to \mathrm{WW^*/WW}$ and $\mathrm{H} \to \mathrm{ZZ^*/ZZ}$ channels, although for $\mathrm{m_H} \gtrsim 2\mathrm{m_{top}}$ the $\mathrm{t\bar{t}}$ branching fraction can be as large as 20%.

In the MSSM the $\mathrm{H, A} \to \mathrm{b\bar{b}}$ decay dominates at large tanβ ($\gtrsim$ 10). In this domain the branching fraction to $\tau^+\tau^-$ is about 10% and that to $\mu^+\mu^-$ about 3×10^{-4}. At small tanβ and large masses the branching fraction to $\mathrm{t\bar{t}}$ can be as large as 90%. For the heavy scalar, the branching fractions for the hh, WW and ZZ decays are below the 10^{-3} level for large tanβ but can reach $\sim$80% for small tanβ. Similarly, for the pseudoscalar A at small tanβ values the branching fraction for $\mathrm{A} \to \gamma\gamma$ is about 2×10^{-4} around $\mathrm{m_A}$ = 200-300 GeV/c^2 and that for the $\mathrm{A} \to \mathrm{hZ}$ decay is $\sim$ 40%. If kinematically allowed the decay fraction to gauginos can reach $\sim$ 20% at large tanβ and $\sim$ 70% at small tanβ. The branching fractions at small tanβ and the thresholds for the decays to gauginos are sensitive to the SUSY parameters.

The light charged Higgs bosons ($\mathrm{m_{H^{\pm}}} < \mathrm{m_{top}}$) decay to $\tau\nu_\tau$ with an almost 100% branching fraction. At large tanβ, the $H^\pm \to tb$ decay dominates for $m_{H^\pm} \gtrsim$ 200 GeV/c^2, the $H^\pm \to \tau\nu_\tau$ branching fraction decreases and is about 10% for $m_{H^\pm} \gtrsim$ 400 GeV/c^2. The other interesting branching fraction $H^\pm \to \mu\nu_\mu$ is at the level of only $\sim 10^{-3}$. The branching fraction for the $H^\pm \to Wh$ decay mode may reach $\sim$ 10% at small tanβ around $m_{H^\pm} \sim$ 200 GeV/c^2. The decay branching fractions to gauginos can reach $\sim$ 10% at large tanβ and $\sim$ 30% at small tanβ, in the SUSY parameter region where gauginos are predicted to be light enough.

2.3 Search strategy

In this section are discussed the search strategies for a light SM-like Higgs boson, a heavy SM Higgs boson, heavy MSSM Higgs bosons and MSSM Higgs bosons in specific SUSY channels, with decays to gauginos and in the production through the gaugino decays. In addition to the Higgs boson mass and decay channel these strategies depend on the production process: the inclusive production, the associated production or the production in the weak gauge boson fusion.

2.3.1 The SM Higgs boson

A light SM-like Higgs boson with $m_H \lesssim$ 150 GeV/c^2 can be searched for in the $H \to \gamma\gamma$, $H \to b\bar{b}$, $H \to ZZ^*/WW^*$, $H \to \tau^+\tau^-$, $H \to \mu^+\mu^-$ and $H \to Z\gamma$ decay channels. In this mass range the small natural width, $\Gamma_H \ll$ 1 GeV, can be exploited by optimizing the mass resolution in the $H \to \gamma\gamma$, $H \to ZZ^* \to \ell^+\ell^-\ell'^+\ell'^-$ and $H \to \mu^+\mu^-$ channels. These channels can be searched for inclusively in the dominant $gg \to H$ production process. In this mode, the jet backgrounds are large for the $H \to \gamma\gamma$ channel, while the $H \to ZZ^* \to \ell^+\ell^-\ell'^+\ell'^-$ channel yields a clean signature with a much lower background. The $H \to \gamma\gamma$ channel can also be searched for in the associated production processes WH and $t\bar{t}H$ with an isolated lepton from $W \to \ell\nu_\ell$ and in the H+jet production with a large E_T hadronic jet. Better signal-to-background ratios are obtained, thereby relaxing the demand on the resolution of the electromagnetic calorimeter, but the event rates are low due to small production cross sections. The large $H \to b\bar{b}$ branching fraction for $m_H \lesssim$ 130 GeV/c^2 can be exploited only in the associated production channels $t\bar{t}H$ and WH due to the large backgrounds from multi-jet events and due to the modest ($\sim$ 11%) Higgs boson mass resolution with the $H \to b\bar{b}$ decay channels. Because of their tiny branching fractions, the $H \to \mu^+\mu^-$ and $H \to Z\gamma$ decay channels may be exploited only with integrated luminosities exceeding 100 fb^{-1}. The gauge boson fusion production, $qq \to qqH$, is shown to be accessible in the mass range $m_H \lesssim$ 150 GeV/c^2 in the $H \to \gamma\gamma$, $H \to WW^*$, $H \to \tau^+\tau^-$ and possibly in the $H \to b\bar{b}$ and $H \to \mu^+\mu^-$ decay modes [12]. Because no colour is exchanged in the central hard process, the gauge boson fusion leads to a low jet activity in the central rapidity region. Detecting the forward jets and imposing a veto on jets in the rapidity range between the forward jets largely reduces the QCD and $t\bar{t}$ backgrounds.

In the mass range from 120 to 200 GeV/c^2, the $H \to WW^*/WW \to \ell^+\nu_\ell\ell^-\nu_\ell$ channel can also be exploited. It requires a good understanding of $t\bar{t}$ and Wtb backgrounds. The event rate is large but only the transverse Higgs boson mass can be reconstructed in this channel due to two neutrinos in the final state. Above 200 GeV/c^2, the $H \to ZZ \to \ell^+\ell^-\ell'^+\ell'^-$ channel yields the highest sensitivity up to 500 GeV/c^2. Above 500 GeV/c^2, where the natural width of the Higgs boson is large, the final states with larger branching fractions including jets and E_T^{miss} from the $H \to ZZ/WW$ decays are used. In this mass range, the cross section for the $qq \to qqH$ production process is large and can be fully exploited.

2.3.2 The heavy neutral MSSM Higgs bosons H and A

The suppression of the couplings to gauge bosons implies different search strategies. At large tanβ, the coupling enhancement to down-type fermions allows searching for the H and A bosons in the H,A $\to \mu^+\mu^-$, H,A $\to \tau^+\tau^-$ and H,A $\to b\bar{b}$ decay channels in the associated production $gg \to b\bar{b}H/A$. In this production process, the associated b jets can be used to suppress the Z, γ^* and QCD multi-jet backgrounds with b-tagging methods. To take advantage of the hadronic τ decays in the lepton-plus-τ-jet and two-τ-jet final states from the H,A $\to \tau^+\tau^-$ decay, an efficient τ-jet identification method is required to suppress further QCD multi-jet and W-plus-jet backgrounds. In the next sections, a τ jet stands for the one or three collimated charged hadrons possibly accompanied by π^o mesons from a $\tau \to$ hadrons + ν_τ decay. The Higgs boson mass can be reconstructed also in the H,A $\to \tau^+\tau^-$ channels from E_T^{miss} and the visible τ momenta exploiting the neutrino collinearity with the parent τ direction. For the H,A $\to b\bar{b}$ decay channel the signal-to-background ratios are low due to overwhelming QCD multi-jet backgrounds. Good understanding of these backgrounds and b tagging are needed already at the high-level trigger.

2.3.3 The charged Higgs bosons

To search for the heavy charged Higgs bosons ($\mathrm{m_{H^\pm}} > \mathrm{m_{top}}$), the $\mathrm{H^\pm} \rightarrow \tau\nu_\tau$, $\mathrm{H^\pm} \rightarrow \mathrm{tb}$ and $\mathrm{H^\pm} \rightarrow \mathrm{Wh}$ decay channels can be used in the associated production process $\mathrm{gg} \rightarrow \mathrm{btH^\pm}$. The $\mathrm{H^\pm} \rightarrow \tau\nu_\tau$ decay channel can be used also in the direct production $\mathrm{q\overline{q}} \rightarrow \mathrm{H^\pm}$. In the associated production process, the W+jet and QCD multi-jet backgrounds can be suppressed with b tagging and reconstruction of the associated top quark. The $\mathrm{H^\pm} \rightarrow \tau\nu_\tau$ decay channel is particularly interesting, when hadronic τ decays are required as: i) the $\mathrm{t\overline{t}}$ and Wt backgrounds with genuine τ's can be suppressed exploiting the different helicity correlations in the $\mathrm{H^\pm} \rightarrow \tau\nu_\tau$ and the $\mathrm{W^\pm} \rightarrow \tau\nu_\tau$ decay channels [13], ii) the transverse Higgs boson mass can be reconstructed allowing the signal and background to be separated. For the $\mathrm{H^\pm} \rightarrow \mathrm{tb}$ decay channel, the $\mathrm{t\overline{t}}$-plus-multijet backgrounds can be reduced only with b tagging, leading to low signal-to-background ratios. The $\mathrm{H^\pm} \rightarrow \mu\nu_\mu$ decay channel may be exploited with integrated luminosities exceeding 100 $\mathrm{fb^{-1}}$. The light charged Higgs bosons ($\mathrm{m_{H^\pm}} < \mathrm{m_{top}}$) can be searched for in the $\mathrm{H^\pm} \rightarrow \tau\nu_\tau$ decay channel in the $\mathrm{t\overline{t}}$ production, suppressing the backgrounds with an isolated lepton from the accompanying W decay. For efficient triggering of the $\mathrm{H^\pm} \rightarrow \tau\nu_\tau$ channel with a single τ jet and of the two-τ-jet final state from H,A $\rightarrow \tau^+\tau^-$, a specific trigger algorithm is needed.

2.3.4 Decays of and into gauginos

The decays into SM particles may provide access to the heavy MSSM Higgs bosons only at large tanβ. The small and medium tanβ values could be partly explored with Higgs boson decays to gauginos. If the gaugino masses are small enough, the branching fractions for the $\mathrm{H,A} \rightarrow \chi_2\chi_2$ and $\mathrm{H^\pm} \rightarrow \chi_{2,3}\chi^\pm_{1,2}$ decays can be sizeable. These decay channels can be searched for in multi-lepton final states if the sleptons are light enough because, for light sleptons, the branching fraction for the $\chi_2 \rightarrow \tilde{\ell}\ell \rightarrow \chi_1\ell^+\ell^-$ decay can be as large as $\sim$ 55%. The Higgs boson mass reconstruction is not possible for these channels due to the invisible neutralinos at the end of the decay chain. The lighter scalar Higgs boson can also be searched for in invisible final states through decays into lightest neutralinos $\mathrm{h} \rightarrow \chi_1\chi_1$, in the gauge boson fusion production.

In the MSSM, Higgs bosons can also be produced as decay products of gauginos in the squark and gluino cascades. More specifically, squarks and gluinos can decay to heavy charginos and neutralinos, $\chi^\pm_2$, χ_3 and χ_4. If kinematically allowed these particles decay into the lighter chargino and neutralinos, $\chi^\pm_1$, χ_1 and χ_2 and Higgs bosons. Squarks and gluinos can also decay directly to the light gauginos $\chi^\pm_1$ and χ_2 which then decay to the lightest neutralino and Higgs bosons. The production rates can be large ($\sim$ 0.3 pb for $\mathrm{m_A} \sim$ 200 GeV/c^2) as the squarks and gluinos are produced via strong interactions. These events are characterized by large $\mathrm{E_T^{miss}}$ and large jet multiplicity. These features can be used to suppress efficiently the SM backgrounds and allow the $\mathrm{h,H,A} \rightarrow \mathrm{b\overline{b}}$ decays to be exploited.

2.4 Influence of MSSM parameters on Higgs boson production and decays

2.4.1 Decays to SUSY particles

The lightest charginos and neutralinos may have masses of the order of the Z boson mass. The heavy CP-even, CP-odd and charged Higgs bosons of the MSSM can therefore decay into these particles. In addition to tanβ and $\mathrm{m_A}$, the masses of charginos and neutralinos as well as their couplings to the Higgs bosons depend on the higgsino mass parameter μ and the gaugino mass parameter $\mathrm{M_2}$.

The MSSM Higgs bosons can decay also into the SUSY partners of leptons and quarks if the latter are light enough. In particular, if kinematically allowed, decays into third generation sfermions can be dominant due to enhanced couplings. The sfermions masses and couplings to Higgs bosons for each generation depend on the left- and right-handed soft SUSY-breaking mass parameters $\mathrm{m_{\tilde{f}_L}}$ and $\mathrm{m_{\tilde{f}_R}}$ and the trilinear coupling $\mathrm{A_t}$ (in addition to tanβ and $\mathrm{m_A}$).

The variation of the H $\rightarrow \tau^+\tau^-$ branching fraction as a function of the MSSM parameters was studied in Ref. [14]. For smaller $|\mu|$ and $\mathrm{M_2}$ the neutralinos become lighter, which increases the branching fractions to these particles for large Higgs boson masses and suppresses the $\mathrm{H} \rightarrow \tau^+\tau^-$ branching fraction. For $\mathrm{m_A}$ = 500 GeV/c^2 and tanβ = 30 the $\mathrm{H} \rightarrow \tau^+\tau^-$ branching fraction decreases by about 20% when μ is decreased from 300 GeV/c^2 to 200 GeV/c^2. Increasing μ from 300 GeV/c^2 to 500 GeV/c^2 enhances this branching fraction by about 15%. These variations are somewhat smaller for negative μ values while they are much larger at smaller tanβ values. The variation as a function of $\mathrm{M_2}$ is about 10% for 120 $< \mathrm{M_2} <$ 300 GeV/c^2. For lighter squarks and gluinos ($\mathrm{M_{\tilde{g}}}$ = $\mathrm{M_{\tilde{q}}}$ = 500 GeV/c^2), the branching fraction is enhanced by $\sim$ 14%. At large tanβ the H,A $\rightarrow \tau^+\tau^-$ and H,A $\rightarrow \mu^+\mu^-$ branching fractions can be affected by stop mixing only if the MSSM mass spectrum is such that the H,A $\rightarrow \tilde{t}\tilde{t}$ decays are allowed.

2.4.2 Higgs boson production

The gluon fusion process, $gg \rightarrow h$, is mediated by loops involving top and bottom quarks as well as squarks. The $h \rightarrow \gamma\gamma$ decay is mediated by W and heavy fermion loops as in the Standard Model and, in addition, by charged Higgs, sfermion and chargino loops. If the stop mixing is large, one of the stop quarks can be light. When the stop mass approaches the top mass the destructive interference between the top and stop contributions in the loops becomes significant. As a consequence, the $gg \rightarrow h$ cross section can be very much reduced while the $h \rightarrow \gamma\gamma$ branching fraction is only slightly enhanced. The net result is a decrease of the overall $gg \rightarrow h \rightarrow \gamma\gamma$ rate [15]. This effect can even preclude the observability in the inclusive $h \rightarrow \gamma\gamma$ and $h \rightarrow ZZ^* \rightarrow \ell^+\ell^-\ell'^+\ell'^-$ channels for $m_{\tilde{t}_1} \lesssim$ 200 GeV/c^2, and reduce the sensitivity in these channels for $m_{\tilde{t}_1} \lesssim$ 300 GeV/c^2 [16]. The discovery potential for the heavy MSSM Higgs bosons is not sensitive to the stop mixing and light stop ($\tilde{t}_1$) mass due to the dominance of associated production (tree diagram) at large tanβ and because the CP-odd Higgs boson does not couple to $\tilde{t}_1\tilde{t}_1$ pair but to $\tilde{t}_1\tilde{t}_2$ ($m_{\tilde{t}_2}$ remains always large, of the order of 1 TeV/c^2).

3 Simulation and reconstruction

3.1 Detector

A detailed description of the CMS detector can be found in Refs. [17-22]. The distinctive features of the detector are a 4T axial magnetic field, a multilayer muon system in the return yoke [17], a scintillating crystal electromagnetic calorimeter (ECAL), a sampling hadron calorimeter (HCAL) and an all-silicon inner tracking system based on fine-grained micro-strip and pixel detectors. The calorimeters and the tracker are located inside the solenoid.

In the original design, the tracking detector [18] consisted of a pixel vertex, a silicon micro-strip detector and MSGC gas detectors in the outer layers. In 2000 a modification of the original design of the tracker was approved [19]. In the new design, the outer MSGC layers are substituted by layers of silicon micro-strips leading to an all-silicon configuration. The layout of the all-silicon tracker was subsequently optimized in terms of performance and cost, before finally being frozen in the fall of 2001. It was ascertained that the two versions of the tracker provide comparable hit reconstruction quality for tracks with $p_T > 2$ GeV/c. The single track reconstruction performance as well as the track reconstruction efficiency in jets are not affected by the change of layout. The pixel detector consists of three barrel layers placed at mean radii of 4.4, 7.3 and 10.2 cm, from the beam axis and two endcap disks on each side. This detector has been designed to give a two-hit coverage up to rapidities of about $|\eta|$ = 2.2 (for tracks originating within 2σ around the centre) for large p_T tracks. The detector occupancy is low due to a small pixel size 150 μm $\times$ 150 μm. The silicon strip tracker is based on micro-strip silicon devices with a thickness between 320 and 500 μm and a pitch size between $\sim$ 80 and $\sim$ 180 μm. This detector consists of the inner barrel of four layers, the outer barrel of six layers, the inner endcap made of three small disks on each side and the outer endcap made of nine large disks on both sides.

The electromagnetic calorimeter [20] is located between the tracker and the hadron calorimeter, and is composed of about 80000 $PbWO_4$ crystals covering the rapidity range up to $|\eta| < 3$. Precise energy measurement for photons and electrons can be performed up to $|\eta| <$ 2.5 except for the region 1.4442 $< |\eta| <$ 1.5660. In the ECAL barrel part the crystals are tilted so that their axes make an angle of 3° with a line from the nominal vertex point. Each of them covers approximately $\Delta\eta \times \Delta\phi$ = 0.0174×0.0174. The crystal length is 230 mm (25.8 X_0). The endcap consists of identically shaped crystals, slightly shorter (220 mm, 24.7 X_0) and somewhat larger in cross-section than the barrel crystals, grouped in mechanical units of 5×5 crystals (super-crystals). The crystals and super-crystals are arranged in a rectangular x-y grid, with the crystal axes off-pointing from the nominal vertex by angles between 2° and 5°. A preshower detector, made of lead radiators (3X_0) and two orthogonal planes of silicon strip detectors, covers most of the endcap calorimeter ($|\eta| >$ 1.653). The energy resolution for a single electromagnetic shower inside the barrel (endcap) measured with a 5×5 crystal array at low luminosity ($10^{33}cm^{-2}s^{-1}$) is σ_E/E = 2.7(5.7)%/$\sqrt{E} \oplus 0.155(0.770)/E \oplus 0.55\%$ (E in GeV) [20].

The sampling hadron calorimeter [21] extends up to $|\eta|$ = 3, and consists of 4 mm thick plastic scintillator tiles inserted between brass absorber plates. The barrel and endcap parts of the calorimeter are placed inside the solenoid. The outer hadron calorimeter is located in the central region of the detector, $|\eta| < 1.305$, outside the solenoid in the barrel return yoke to measure the late shower development. The lateral granularity of the calorimeter towers is $\Delta\eta \times \Delta\phi$ = 0.087 $\times$ 0.087 for $|\eta| < 2$. The calorimeter readout has a dynamic range from 5 MeV to 3 TeV to allow single muons to be observed. Test beam studies with a full ECAL+HCAL prototype indicate that an energy resolution of σ_E/E = 112%/$\sqrt{E} \oplus$ 3.6% (E in GeV) is achievable for single pions with energies between 20 GeV and 300 GeV [21]. To extend the hermeticity of the hadron calorimeter up to $|\eta|$ = 5.191, a separate forward calorimeter is placed at a distance of 11 m from the interaction point. This calorimeter, situated in a high radiation and high rate environment, uses quartz fibers as an active medium, embedded in the iron absorber wedges.

The muon system [22] consists of four stations of muon chambers with excellent time resolution in the central barrel and in the endcap regions and provides a hermetic coverage up to $|\eta| < 2.4$. The system is based on drift tubes in the barrel region, cathode strip chambers in the endcap regions and resistive plate chambers in both barrel and endcap regions. The time-tagging capability of the drift tubes allows bunch crossings to be identified. The cathode strip chambers in the endcap regions are capable to give precise spatial and timing information in the presence of strong magnetic field and large particle rate. The muon system, operating inside the magnetic field return, gives a standalone muon momentum measurement, essential for the first level (Level-1) trigger and useful for the matching between the muon system and the tracker at the High Level Trigger (HLT).

The detector is assumed to be properly calibrated and aligned for the studies presented in this work. For the pixel and silicon strip detectors an alignment with an accuracy of about 10 μm in all three dimensions is required. The ultimate momentum resolution for very high p_T muons ($p_T > 200$ GeV/c^2) is reached with a ~ 100 μm alignment of the muon system with respect to the tracker.

To simulate the detector, a GEANT-based detector simulation package CMSIM [23] and a fast detector simulation package CMSJET [24] with parametrizations from full detector simulations were used. In particular, a fast tracker response simulation [25] was made on the basis of the full simulation of the silicon-MSGC tracker design [18]. The energy resolution of the electrons, photons and hadrons corresponds to what has been obtained from full simulations in Refs. [20, 21]. Transverse and longitudinal shower development in the calorimeter was simulated as well as effects of the main gaps with dead materials.

3.2 Trigger

Detailed descriptions of the Level-1 and HLT triggers can be found in Refs. [26, 27]. Trigger simulations are also presented in detail in these references. The allowed Level-1 trigger bandwidth is 16 kHz (33 kHz) at low (high) luminosity. An equal allocation was assumed across the four categories of objects, taken as (a) electrons/photons, (b) muons, (c) τ jets and (d) jets, jet-plus-electron, jet-plus-muon and jet-plus-E_T^{miss}. Thresholds for the single and double-object triggers were optimized for a given rate using selected physics channels. For the single and double τ triggers, the efficiency for the $A \to \tau^+\tau^-$ channel versus the efficiency for the $H^\pm \to \tau\nu_\tau$ channel was used. For the electron/photon trigger, the $W \to e\nu_e$ and $Z \to e^+e^-$ channels were considered.

A method of partial event reconstruction is used for the HLT online event selections running in the Filter Farm exploiting muon, calorimeter and tracker data to identify the physics objects. Calorimeter, tracker matching and isolation techniques are used to select τ jets, muons, electrons and photons. Cuts on the η separation between two jets are used at the HLT to trigger for invisible Higgs boson decays in the $qq \to qqh$ process. For a single jet, b tagging with track impact parameter measurement is possible at the HLT. The HLT output rate is ~ 100 Hz. At low luminosity the E_T or p_T thresholds corresponding to a 95% efficiency are 29 (17) GeV for single (double) electron; 80 (40, 25) GeV for single (double) photons; 19 (7) GeV/c for single (double) muons (90% efficiency); 86 (59) GeV for single (double) τ jets; 180 GeV for jet and 123 GeV for E_T^{miss} in the jet-plus-E_T^{miss} trigger; 19 GeV for electron and 45 GeV for τ jet in the electron-plus-τ jet trigger. For some studies described in this paper somewhat different trigger thresholds were taken. For the $H \to ZZ^{(*)} \to \ell^+\ell^-\ell'^+\ell'^-$ channel, for example, asymmetrical thresholds of 20 and 15 GeV were taken for the double electron trigger. The $t\bar{t}H$, $H \to b\bar{b}$ channel was assumed to be triggered with a single lepton with $p_T \geq 10$ GeV/c. In the latest design the η range of the muon trigger is up to $|\eta| \leq 2.1$. These changes, however, have a small effect on the discovery potential. Full trigger simulation is already included in the studies for the channels like the $H/A \to \tau^+\tau^- \to$ two jets and the invisible Higgs boson decays from the $qq \to qqh$ production process.

3.3 Reconstruction

3.3.1 Photons

A detailed description of the photon and $H \to \gamma\gamma$ reconstruction can be found in Refs. [20] and [28]. The photon conversions in the tracker material can degrade the Higgs boson mass resolution and can lead to event losses. The studies for the $H \to \gamma\gamma$ channel were performed with a tracker design where about 24% (35%) of photons convert in the tracker volume in front of the barrel (endcap) ECAL. A matrix of 5 $\times$ 5 crystals is used to measure the energy of non-converted photons. Dedicated algorithms have been developed to identify and reconstruct the converted photons in the calorimeter. About 6% of the photon conversions are not recoverable. The hadronic jets misidentified as single photons are first suppressed with isolation cuts in the tracker keeping the photon efficiency at 95%. Rejection of the neutral isolated pions is performed using the lateral shower shape measured in the crystals in the barrel part and the preshower detector in the endcap parts of the calorimeter. For $\mathrm{p_T^{\pi^0}}$ = 40 GeV/c, for instance, about 70% of the π^0's are rejected in the barrel region and about 55% in the endcaps for a 90% efficiency for single photon. The reconstruction and selection efficiency for a single photon from H$\rightarrow \gamma\gamma$ is estimated to be 74%. The inefficiency consists of losses in the fiducial area of the electromagnetic calorimeter (7.5%), lost conversions (6%), losses due to the isolation requirements (5%) and losses due to the π^0 rejection (10%). The events in which a Higgs boson is produced contain more large-$\mathrm{p_T}$ tracks than minimum-bias pileup events. This feature is exploited to find the vertex for the $\mathrm{H} \rightarrow \gamma\gamma$ mass reconstruction. The efficiency and the purity of this method depends in particular on the minimum-bias event model and on the $\mathrm{p_T}$ spectrum of the Higgs boson as well as on the luminosity. The Higgs boson mass resolution (σ of the gaussian fit) is 0.65 (0.69) GeV/c^2 at low (high) instantaneous luminosity for $\mathrm{m_H}$ = 100 GeV/c^2. A mass window of $\pm1.4\sigma$ contains 73% of events at low luminosity and 69% at high luminosity.

3.3.2 Electrons

An electron is identified as an ECAL cluster associated with a track in the inner detector. Before reaching the ECAL, electrons radiate in the material between the interaction point and the ECAL. For example, for electrons with $\mathrm{p_T}$ = 35 GeV/c and $|\eta| \leq 1.5$, the mean energy loss is 43.6% before exiting the tracker volume [29] in the tracker design described in Ref. [19]. This corresponds to an average $0.57\mathrm{X_0}$ of material. Most of the energy is radiated as quasi-collinear low energy photons. The bending of the electron in the 4 T magnetic field results in a spray of energy reaching the ECAL. The distribution of this energy is, to a good approximation, only in the φ direction. Bremsstrahlung recovery algorithms, based on an asymmetrical crystal window [30] or on more dedicated clustering methods [29, 31], have been developed. The energy resolution for electrons with $\mathrm{p_T}$ = 35 GeV/c in the barrel is 1.2 (1.5)% for low (high) luminosity [27]. The angular resolution in φ is 1.7 (1.9) mrad and in η it is 1.1×10^{-3}. The electron reconstruction efficiency in the tracker for $\mathrm{p_T^e} \geq$ 10 GeV/c is greater than 90% even in the η regions with the largest number of $\mathrm{X_0}$ [18]. An algorithm for electron momentum measurement in the tracker taking into account bremsstrahlung energy losses is under development [32]. The $\mathrm{H} \rightarrow \mathrm{ZZ}^* \rightarrow \mathrm{e^+e^-e^+e^-}$ channel was studied in Refs. [31, 33, 34] using somewhat different reconstruction algorithms and assumptions for the ECAL energy resolution and tracker design. The Higgs boson mass resolution, still with the silicon-MSGC tracker version, was found at low luminosity to be 1.3, 1.6 and 1.8 GeV/c^2 for $\mathrm{m_H}$ = 130, 150, 170 GeV/c^2, respectively, and the 67% of events were found within $\pm\, 2\sigma$ [31]. Studies with the latest tracker design with about 30% more material are in progress.

3.3.3 Muons

The muon $\mathrm{p_T}$ is measured with a precision of $\sim$ 1% up to $\mathrm{p_T} \sim$ 100 GeV/c in the barrel part of the tracker. The average Level-1 plus HLT reconstruction efficiency is 97% for muons within $5 < \mathrm{p_T} < 100$ GeV/c and $|\eta| < 2.1$ [27]. The discovery potential for the $\mathrm{H} \rightarrow \mathrm{ZZ}^{(*)} \rightarrow \ell^+\ell^-\ell'^+\ell'^-$ channel in Refs. [33, 35] was evaluated with an early tracker version. The Higgs boson mass resolution in the four-muon decay mode was found to be 0.8 and 0.9 GeV/c^2 for $\mathrm{m_H}$ = 130 and 150 GeV/c^2, respectively [22, 35]. These resolutions are somewhat better than those from the preliminary simulations with the present tracker design. The single muon reconstruction efficiency was taken to be 90%, which is lower than that of Ref. [27]. Due to the compensation of these two factors no sizeable change is expected for the discovery potential for the $\mathrm{H} \rightarrow \mathrm{ZZ}^{(*)} \rightarrow \mu^+\mu^-\mu^+\mu^-$ and $\mathrm{H/A} \rightarrow \mu^+\mu^-$ channels.

3.3.4 Jets

Reconstruction of hadronic jets is performed with an iterative cone algorithm [36], with a cone size of 0.5, and taking as input the energy and (η,φ) position of the calorimeter towers. Jet energy corrections take into account the non-linear response to hadrons, out-of-cone energy leakage due to magnetic field and showering and energy offset due to pile up and one-sided zero-suppression (only those channels that are above a threshold are read out). Energy corrections are derived from Monte Carlo data by comparing the energy of jets obtained from the generator-level particles in the hard interaction to that of jets reconstructed in the calorimeter with the same cone size. In the latest simulations [27] the stochastic and constant terms of the jet transverse energy resolution for low luminosity are 1.18 and 0.07. This resolution is $\sim$ 20% worse than those used for some studies in this paper, in particular for the study of the $\mathrm{t\bar{t}H}$, $\mathrm{H} \rightarrow \mathrm{b\bar{b}}$ channel. However, further improvements are expected for the jet resolution and energy scale from the jet energy corrections with charged particles [37]. For many channels, in particular for the gauge boson fusion channels, a central jet veto was used to suppress backgrounds. An $\mathrm{E_T}$ threshold of $\sim$ 20 GeV can be used for these jets as the full simulation studies [38] show that a jet initiated by a parton with $\mathrm{p_T}$ = 20 GeV/c can be found in the calorimeter with an efficiency of $\sim$ 70% at high luminosity ($10^{34}\mathrm{cm}^2\mathrm{s}^{-1}$) with an algorithm where the pile-up energy from on the average of 17.3 minimum bias interactions is subtracted on an event-by-event basis.

3.3.5 Missing transverse energy

Measurement of the missing transverse energy ($\mathrm{E_T^{miss}}$) is affected by the non-linear calorimeter response. A method to improve the $\mathrm{E_T^{miss}}$ scale using jet energy corrections was developed in Ref. [39]. A significant improvement was obtained for the Higgs boson mass resolution and the reconstruction efficiency in the $\mathrm{H} \rightarrow \tau^+\tau^-$ channel. Despite the escaping neutrinos, the Higgs boson mass can be reconstructed in the $\mathrm{H} \rightarrow \tau^+\tau^-$ channels from the visible τ momenta (leptons or τ jets) and $\mathrm{E_T^{miss}}$ with the collinearity approximation for the neutrinos from highly boosted τ's. The correction of the missing $\mathrm{E_T}$ scale improves the reconstruction efficiency by reducing the number of events with negative reconstructed τ energies. The mass resolution depends on the angle $\Delta\varphi$ between the visible τ momenta as 1/sin($\Delta\varphi$) and is sensitive to the $\mathrm{E_T^{miss}}$ measurement, both in magnitude and particularly in direction. Figure 3 [39] shows the Higgs boson mass reconstructed with full simulation for the fully hadronic final state from $\mathrm{H} \rightarrow \tau^+\tau^- \rightarrow$ two τ jets for $\mathrm{m_A}$ = 500 GeV/c^2 with the jet energy corrections. The reconstruction efficiency (including the cut $\Delta\varphi < 175°$) is around 35% for $\mathrm{m_A}$ = 200 and 500 GeV/c^2. This efficiency, obtained with an $\mathrm{E_T^{miss}}$ cut, is improved by a factor of about two when a b jet is required in the event, mainly due to a more efficient $\Delta\varphi$ cut [14]. A mass resolution around 15% is obtained for $\mathrm{m_A}$ = 200 and 500 GeV/c^2 with the cut $\Delta\varphi < 175°$. Energy-flow algorithms are expected to further improve the $\mathrm{E_T^{miss}}$ measurement.

3.3.6 τ identification

The τ-jet identification takes advantage of the τ-jet properties such as narrowness and low multiplicity. A hadronic τ decay produces an energy deposit in the calorimeter narrower than that from an average hadronic jet. On average, 85% of the τ-jet energy is contained in a 3 $\times$ 3 trigger cell corresponding to a cone size of about 0.1 and 98% in a cone of 0.4 for $\mathrm{E_T^{\tau\ jet}} > 40$ GeV [40, 41]. These features are used in the Level-1 trigger [27] where transverse profiles of the active tower patterns are analysed to tag narrow jets as potential hadronic τ decays. A τ jet leads to a localized energy deposit in the electromagnetic calorimeter [41, 42, 43], which can be used in the Level-2 trigger to confirm the Level-1 τ-jet candidates. In the HLT algorithms, loose isolation criteria are used in the tracker [44, 45]. At this level, no requirement is made on the number of tracks in the signal cone, to keep one-, three- (and five-) prong τ decays. Offline τ-jet selections are based on a cut on the $\mathrm{p_T}$ of the leading charged particle, the number

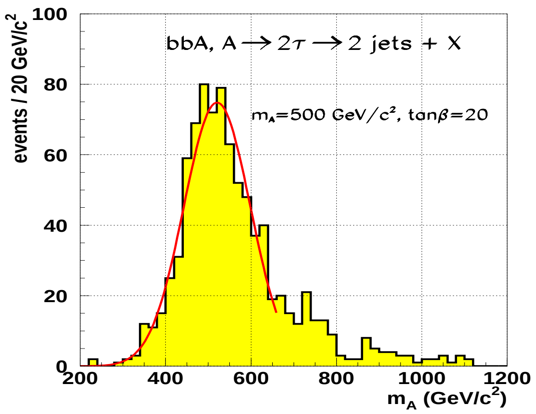

Figure 3: Higgs boson mass reconstructed with full simulation for the $\mathrm{H, A} \rightarrow \tau^+\tau^- \rightarrow$ two jet channel for $\mathrm{m_A}$ = 500 GeV/c^2, tanβ = 20 at low luminosity.

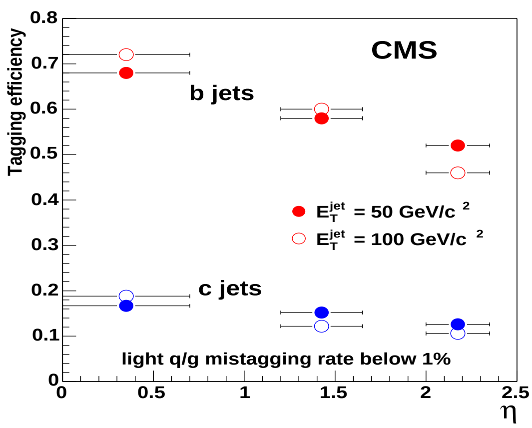

Figure 4: Tagging efficiencies for b and c jets with $\mathrm{E_T^{jet}}$ = 50 and 100 GeV for a 10^{-3} mistagging rate for light quark jets. A track counting method with impact parameter measurement is used.

of charged particles in the signal cone and a signal cone size ($\Delta r < 0.04$) smaller than that used at the HLT. In the study of the $H, A \to \tau^+\tau^-$ channel with lepton-plus-τ-jet final state [46], one prong hadronic τ decays were selected with $p_T > 10$ GeV/c for the single track in the τ jet. The τ-jet selection efficiency in this channel for $E_T^{jet} > 40$ GeV was found to be 0.32 (0.36) for m_A = 140 (300) GeV/c^2 and the misidentification efficiency for the jets from the W + jet background 2×10^{-3} [42]. In the study of the two-τ-jet final state from the $H, A \to \tau^+\tau^-$ channel [14], a high momentum particle with $p_T \geq 40$ GeV/c was required in the core of the jet and for the signal cone around the leading charged particle direction Δr = 0.03 - 0.04 was taken (Δr = 0.07 at the trigger level). The track isolation was performed in the area limited by the signal cone and the isolation cone (Δr = 0.4). If one or three charged particles are required in the signal cone, the efficiency of the τ-jet selection, including the Level-1 and the HLT trigger efficiency, was found to be 0.8% and 9% for m_A = 200 and 500 GeV/c^2, respectively. A rejection factor of about 1000 per jet was obtained. Highly energetic hadronic jets can be further suppressed with an additional cut in p_T^{track}/E_T^{jet} with a small loss of signal efficiency. The τ lifetime can be exploited with the impact parameter measurement to reduce the $Z \to \ell^+\ell^-$ background to $H, A \to \tau^+\tau^- \to \ell^+\ell^- + X$ and to further reduce the QCD multi-jet background for $H, A \to \tau^+\tau^- \to \text{two } \tau \text{ jets} + X$ [47]. A rejection factor of at least 9 was obtained against the QCD multi-jet background with an efficiency of $\sim$ 60% for the $H, A \to \tau^+\tau^-$ events when the charge correlation between the τ jets was also included [14]. For the tree-prong τ decays, secondary vertex reconstruction can be used to reduce more efficiently the hadronic jet background.

3.3.7 Tagging of b jets

The b-jet tagging is performed with the reconstruction of the secondary vertices or with impact parameter measurement. The precision of the impact parameter measurement in the transverse plane is $\sim$ 10 μm for p_T = 100 GeV/c and $\sim$100 μm for p_T = 1 GeV/c. Unless stated otherwise, the tagging probability is calculated by requiring two tracks with $p_T > 1$ GeV/c and $\sigma_{ip} > 2$ inside the jet cone, where σ_{ip} is the significance of the track impact parameter in the transverse plane. Efficiencies to tag b and c jets for E_T^{jet} = 50 and 100 GeV with a 1% mistagging probability for light quark and gluon jets are shown in Fig. 4 as a function of $|\eta^{jet}|$ from a full simulation and complete reconstruction study with the final tracker design [48]. The efficiency to tag b jets, $\simeq$ 70 % ($\simeq$ 50 %) for the barrel (endcap) part of the tracker is about 20% higher than that used for the studies in this paper.

3.4 Signal and background simulation

The PYTHIA Monte-Carlo program [49] was used to generate signal and background events unless stated otherwise. The HERWIG [50] generator was used for the Higgs boson production from gaugino decays and in the study of charged Higgs bosons decaying to gauginos. The MSSM sparticle spectrum and decay branching fractions were calculated with ISASUSY 7.58 [51] (interfaced to HERWIG). The CompHEP program [52] was used to generate higher-order background processes such as: $t\bar{t}jj$ and $t\bar{t}b\bar{b}$, $t\bar{t}j$, electroweak Zjj and Wjj. The CompHEP program was interfaced with PYTHIA for fragmentation and hadronization [53]. The QCD Zjj and Wjj backgrounds were generated with the programs based on the work of Ref. [54] and interfaced to PYTHIA. The signal and all backgrounds for the exclusive $H \to \gamma\gamma$ channels in the H+jet, $qq \to qqH$ and WH production processes were generated with CompHEP. The evaluation of the γ-plus-three-jet background is in progress with CompHEP.

The helicity correlations in the $H^\pm \to \tau\nu_\tau$ and $W^\pm \to \tau\nu_\tau$ decays were accounted for by the TAUOLA package [55]. The production cross sections and branching fractions for the two-τ-jet and two-lepton final states from the $gg \to b\bar{b}H/A$, $H/A \to \tau^+\tau^-$ processes and the branching fractions for the $gb \to tH^\pm$, $H^\pm \to \tau\nu_\tau$ channel were calculated with the programs of Refs. [6, 11]. The LO production cross section for the $gb \to tH^\pm$ process was taken from Ref. [7]. The cross sections and branching fractions for the lighter scalar MSSM Higgs boson were also calculated with the programs of Refs. [6, 11].

Simple sequential cut-based analysis were used. The expected statistical significance was calculated using Poisson statistics for the channels where backgrounds are below $\sim$ 20 events and approximated otherwise by $N_S/\sqrt{N_B}$, where N_S and N_B are the numbers of the signal and background events, respectively. Systematic uncertainties on the background evaluations were not taken into account in the calculation of the statistical significance. A combined statistical significance was calculated as a quadratic sum of the individual significance.

The NLO production cross sections were used for both signal and backgrounds in the inclusive $H \to \gamma\gamma$ channel and in the $H \to ZZ^*/ZZ \to \ell^+\ell^-\ell'^+\ell'^-$ and $H \to WW^*/WW \to \ell\ell\nu_\ell\nu_\ell$ channels. The cross sections and k factors can be found in Ref. [20] for the inclusive $H \to \gamma\gamma$ channel, in Ref. [28] for the $H \to ZZ^*/ZZ \to \ell^+\ell^-\ell'^+\ell'^-$ channel and in Ref. [56] for the $H \to WW^*/WW \to \ell\ell\nu_\ell\nu_\ell$ channel.

4 Standard searches

4.1 Searches for a SM-like scalar Higgs boson H

Figure 5 shows the reconstructed four-lepton invariant mass distribution of the $\mathrm{H} \rightarrow \mathrm{ZZ}^* \rightarrow \ell^+\ell^-\ell'^+\ell'^-$ signal and the background with $\mathrm{m_H}$ = 130, 150 and 170 GeV/c^2 for a luminosity of 100 fb^{-1} [33]. Backgrounds from the ZZ^*, $\mathrm{t\bar{t}}$ and $\mathrm{Zb\bar{b}}$ processes were suppressed by requiring the leptons to be isolated in the tracker, with an upper bound on the lepton impact parameter significance and with cuts on the two-lepton and four-lepton invariant masses. For the largest $\mathrm{p_T}$ electron or muon, $\mathrm{p_T} > 20$ GeV/c was required, the threshold for the second-largest-$\mathrm{p_T}$ electron (muon) was taken to be 15(10) GeV/c and the thresholds for the other two electrons (muons) were taken to be 10(5) GeV/c. For isolated leptons within $|\eta^\ell| < 2.5$ these thresholds lead to a four-electron acceptance of 33% and a four-muon acceptance of 41% for $\mathrm{m_H}$ = 130-150 GeV/c^2. The four-electron final state was studied with full simulation and complete reconstruction [31]. The reconstructed four-electron invariant mass distribution of the $\mathrm{H} \rightarrow \mathrm{ZZ}^* \rightarrow \mathrm{e^+e^-e^+e^-}$ signal and the background with $\mathrm{m_H}$ = 130, 150 and 170 GeV/c^2 for 100 fb^{-1} is shown in Fig. 6.

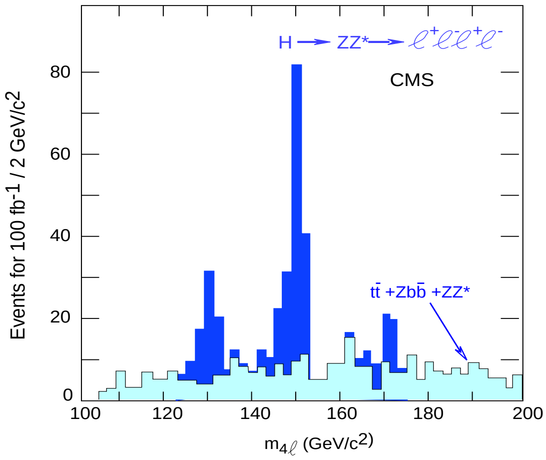

Figure 5: Reconstructed four-lepton invariant mass distribution of the $\mathrm{H} \rightarrow \mathrm{ZZ}^* \rightarrow \ell^+\ell^-\ell'^+\ell'^-$ signal (dark) and the background (light) with $\mathrm{m_H}$ = 130, 150 and 170 GeV/c^2 for 100 fb^{-1} (LO cross sections are assumed).

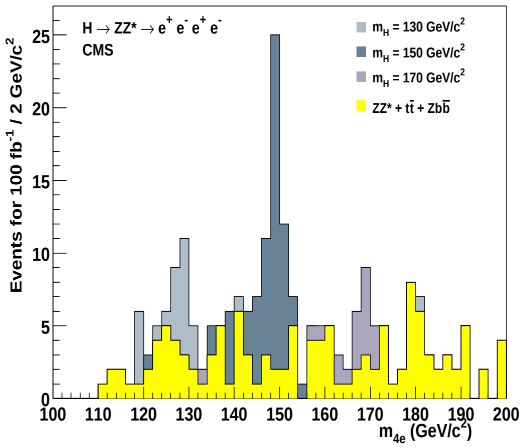

Figure 6: Reconstructed four-electron invariant mass distribution of the $\mathrm{H} \rightarrow \mathrm{ZZ}^* \rightarrow \mathrm{e^+e^-e^+e^-}$ signal (dark) and the background (light) with $\mathrm{m_H}$ = 130, 150 and 170 GeV/c^2 for 100 fb^{-1} with k factors for both signal and background.

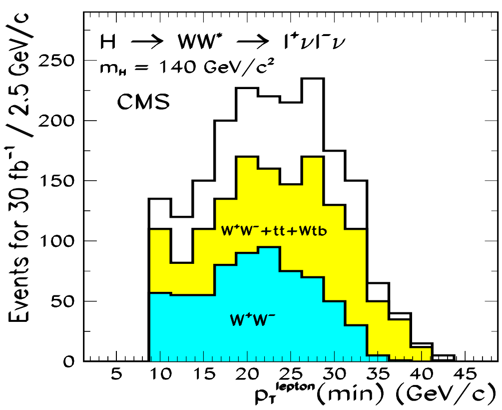

Figure 7: The $\mathrm{p_T}$ distribution of the smaller $\mathrm{p_T}$ lepton of the $\mathrm{H} \rightarrow \mathrm{WW}^* \rightarrow \ell^+\nu_\ell\ell^-\nu_\ell$ signal (white), in the total background (light) and in the $\mathrm{W^+W^-}$ background (dark) with $\mathrm{m_H}$ = 140 GeV/c^2 for 30 fb^{-1} with k factors for both signal and background.

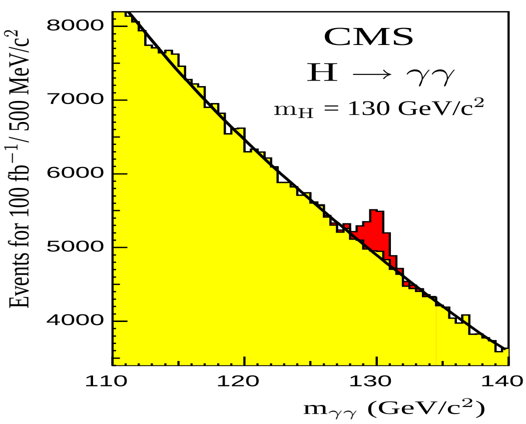

Figure 8: Reconstructed di-photon invariant mass distribution of the $\mathrm{H} \rightarrow \gamma\gamma$ signal (dark) and the background (light) with $\mathrm{m_H}$ = 130 GeV/c^2 for 100 fb^{-1} with k factors for both signal and background.

Around $m_H \sim 170$ GeV/c^2, where the $H \rightarrow ZZ^*/ZZ$ branching fraction is smallest, the $H \rightarrow WW^*/WW \rightarrow \ell^+\nu_\ell\ell^-\nu_\ell$ channel was exploited [56, 57]. For $m_H \lesssim 200$ GeV/c^2, the backgrounds from the $WbW\bar{b}$ and WW production were suppressed by taking advantage of WW spin correlations, which turn into small $\ell^+\ell^-$ opening angles. For $m_H \gtrsim 200$ GeV/c^2, a cut in the transverse momentum of the lepton-pair was used. Central-jet vetoing was used to suppress further the $WbW\bar{b}$ background. Figure 7 shows the distribution of the p_T of the smaller-p_T lepton of the $H \rightarrow WW^* \rightarrow \ell^+\nu_\ell\ell^-\nu_\ell$ signal, the total background and the WW background for a 30-45 GeV/c window in the p_T of the larger p_T lepton with m_H = 140 GeV/c^2 for 30 fb^{-1}. The NLO cross sections were used for both signal and background.

Figure 8 shows the reconstructed di-photon invariant mass distribution of the inclusive $H \rightarrow \gamma\gamma$ signal and the background with m_H = 130 GeV/c^2 for 100 fb^{-1}. The background includes the irreducible direct $pp \rightarrow \gamma\gamma + X$ production and the $pp \rightarrow \gamma + \mathrm{jet} + X$ production with a hard bremsstrahlung from a quark jet [20]. The QCD multi-jet background and the γ-plus-jet background with the jet fragmenting into a leading isolated π^0 were not included. Preliminary full simulation studies with all backgrounds included indicate that these backgrounds are at the level of 40% of the total background. In this inclusive search the signal-to-background ratio is of the order 1/10. In Fig. 8, k factors are used for the signal and for the backgrounds. The $H \rightarrow \gamma\gamma$ decay channel was studied in Ref. [58] in the exclusive production processes, $pp \rightarrow H + \mathrm{jet} + X$, where the Higgs boson is produced at large p_T, and in the associated WH production channel with one isolated lepton from $W \rightarrow \ell\nu_\ell$. Due to an efficient background suppression for these channels, a two-photon mass window of 3 GeV/c^2 was taken instead of the $\pm 1.4\sigma$ (1.9 GeV/c^2) window used for the inclusive $H \rightarrow \gamma\gamma$ search. As the $gg \rightarrow \gamma\gamma g$ background has been found to be small [59], it was not included in the study of Ref. [58]. To further suppress the backgrounds for the $pp \rightarrow H + \mathrm{jet} + X$ channel, a reconstructed partonic centre-of-mass energy in excess of 300 GeV was required in addition to the jet requirements. The $t\bar{t}H$ production channel represents about 35% of the total $\gamma\gamma + \mathrm{lepton}$ production but, to include this component, a complete calculation of the irreducible background from $t\bar{t}\gamma\gamma$ is needed.

Figure 9 shows the invariant mass distribution reconstructed from two b jets in the $t\bar{t}H \rightarrow \ell^\pm\nu_\ell q\bar{q}b\bar{b}b\bar{b}$ signal and in the background with m_H = 115 GeV/c^2 for 30 fb^{-1} [60]. The background includes the $t\bar{t}$+jets, $t\bar{t}b\bar{b}$ and W+jets processes. The correct event configuration among all possible combinations was first searched for to reconstruct the Higgs boson mass. The best configuration was defined as the one giving the highest value for an event likelihood function including b-tagging efficiencies for four jets, probabilities for two jets to be non-b jets, W mass reconstructions and reconstruction of one hadronically and one leptonically decaying top quark. The backgrounds were suppressed with cuts in the likelihood functions for resonances, b tagging and kinematics. Angular correlations between one of the top quarks and the reconstructed Higgs boson were used in Ref. [61]

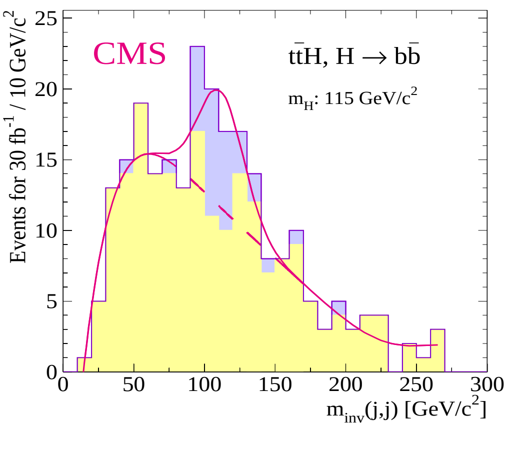

Figure 9: Jet-jet invariant mass distribution of the $t\bar{t}H \rightarrow \ell^\pm\nu_\ell q\bar{q}b\bar{b}b\bar{b}$ signal (dark) and the background (light) with m_H = 115 GeV/c^2 for 30 fb^{-1}.

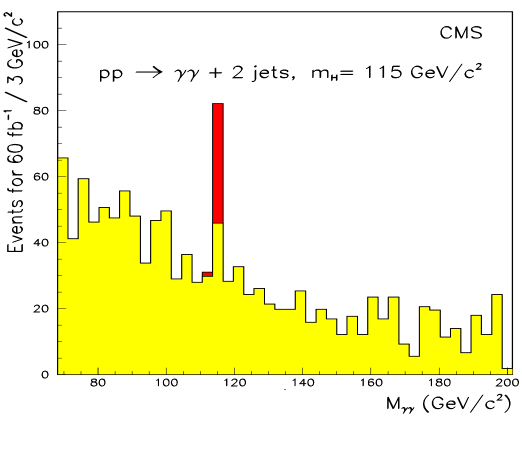

Figure 10: Reconstructed di-photon invariant mass distribution of the $qq \rightarrow qqH$, $H \rightarrow \gamma\gamma$ signal (dark) and the background (light) with m_H = 115 GeV/c^2 for 60 fb^{-1}.

to further reduce the $t\bar{t}b\bar{b}$ background. Fully hadronic final states from the $t\bar{t}H \rightarrow q\bar{q}qqb\bar{b}b\bar{b}$ channel roughly double the number of $t\bar{t}H$ signal events [62]. To study this channel an evaluation of the higher order QCD multi-jet (eight jets) background is still needed. The $WH \rightarrow \ell^{\pm}\nu_\ell b\bar{b}$ channel was studied only for the high luminosity scenario due to the small event rate and many large backgrounds ($W^{\pm}$jj, WZ, $Wt\bar{t}$,tb) [60].

The gauge boson fusion production was studied in the $H \rightarrow \gamma\gamma$, $H \rightarrow WW^*$ and $H \rightarrow \tau^+\tau^-$ decay channels [63, 64, 65]. Figure 10 shows the reconstructed di-photon invariant mass distribution of the $qq \rightarrow qqH$, $H \rightarrow \gamma\gamma$ signal and the irreducible $\gamma\gamma$jj background with m_H = 115 GeV/c^2 for 60 fb^{-1}. The reducible backgrounds have not been evaluated yet for this channel. As for the associated $H \rightarrow \gamma\gamma$ channels, a two photon invariant mass window of 3 GeV/c^2 was taken. The two-lepton-plus-E_T^{miss} final states from the $H \rightarrow WW^* \rightarrow \ell\nu_\ell\ell\nu_\ell$ channel were studied with full simulation for the signal and for the $t\bar{t}$-plus-jet background for m_H = 120 GeV/c^2, for which the $H \rightarrow WW^*$ branching fraction is small [64]. The WW spin correlations were used to suppress the backgrounds. For the $H \rightarrow \tau^+\tau^-$ decay modes the lepton-plus-τ-jet final states were studied [65]. For this channel the mass resolution is crucial due to dominant QCD and electroweak Zjj backgrounds with $Z \rightarrow \tau^+\tau^-$ decays. Figure 11 shows the invariant mass distribution reconstructed from the τ jet, lepton and E_T^{miss} in lepton-plus-τ-jet final state of the $H \rightarrow \tau^+\tau^-$ signal (dark) and the background (light) for m_H = 135 GeV/c^2 with 30 fb^{-1}. For this point the mass resolution was found to be 11.3 GeV/c^2. The W-plus-three-jet background was suppressed with the τ-jet identification criteria.

For Higgs boson masses larger than 500 GeV/c^2 the $H \rightarrow WW/ZZ$ decay modes were used in the gauge boson fusion production process [66, 67]. The $\ell\nu_\ell$jj and $\ell\ell\nu_\ell\nu_\ell$ final states were found to yield the highest sensitivity. The discovery potential can be extended down to $m_H \sim$ 300 GeV/c^2 with the $H \rightarrow WW \rightarrow \ell\nu_\ell$jj channel.

The statistical significance for the SM Higgs boson for 30 fb^{-1} is shown in Fig. 12 for the Higgs boson mass range from 100 to 800 GeV/c^2 and in Fig. 13 in all individual channels for $m_H \leq 150$ GeV/c^2. In these figures, k factors are used for the signal and for the backgrounds in the inclusive $H \rightarrow \gamma\gamma$ channel, in the $H \rightarrow \gamma\gamma$ channel in the H+jet production and in the $H \rightarrow ZZ^*/ZZ \rightarrow \ell^+\ell^-\ell'^+\ell'^-$ and $H \rightarrow WW^*/WW \rightarrow \ell\ell\nu_\ell\nu_\ell$ channels. The statistical significance shown for the gauge boson fusion production channels in Fig. 12 is obtained as a combination of the significance for the $H \rightarrow \gamma\gamma$ and $H \rightarrow \tau^+\tau^-$ channels. The exclusive $H \rightarrow \gamma\gamma$ channels, $\gamma\gamma$-plus-lepton and $\gamma\gamma$-plus-jet, are not included in the total statistical significance in Fig. 12.

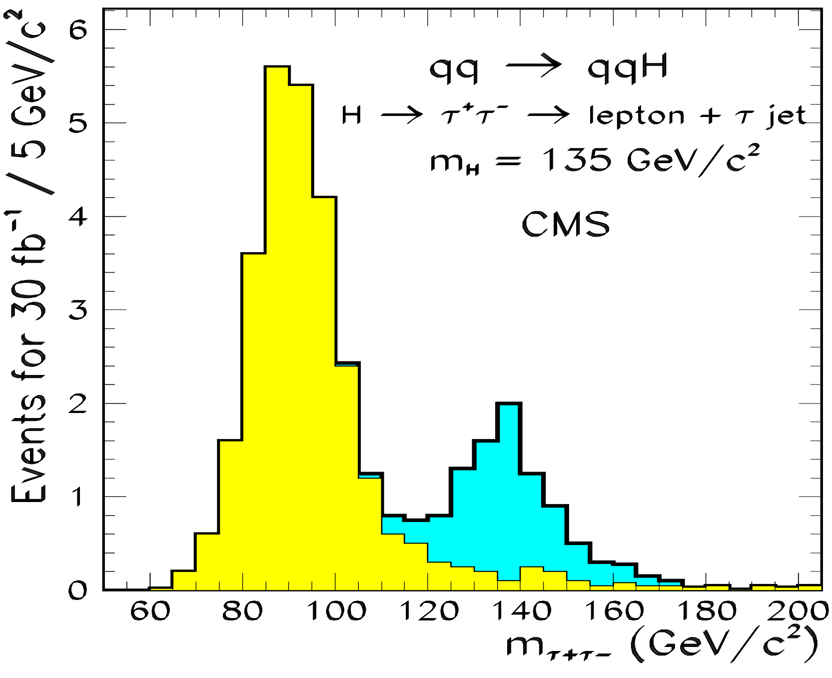

Figure 11: Reconstructed $\tau\tau$ invariant mass distribution in the lepton-plus-τ jet final state in the $qq \rightarrow qqH$, $H \rightarrow \tau^+\tau^-$ signal (dark) and in the background (light) with m_H = 135 GeV/c^2 for 30 fb^{-1}.

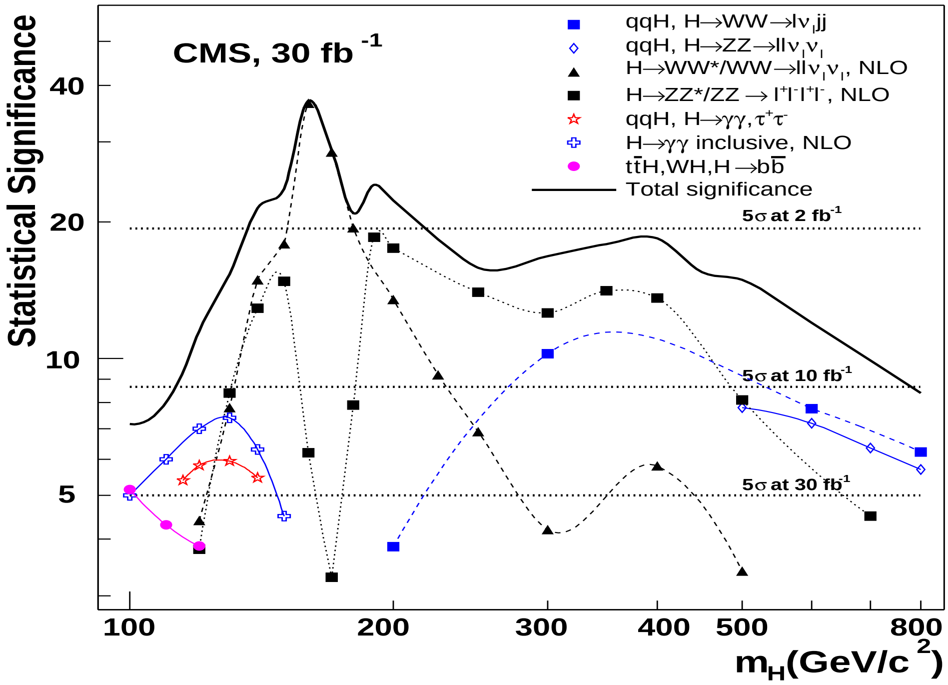

Figure 12: Expected statistical significance with 30 fb^{-1} for the SM Higgs boson as a function of $\mathrm{m_H}$. The NLO cross sections for both signal and background were used for the inclusive $\mathrm{H} \to \gamma\gamma$, $\mathrm{H} \to \mathrm{ZZ}^*/\mathrm{ZZ} \to \ell^+\ell^-\ell'^+\ell'^-$ and $\mathrm{H} \to \mathrm{WW}^*/\mathrm{WW} \to \ell\ell\nu_\ell\nu_\ell$ channels. Poisson statistics were used to calculate the statistical significance for the $\mathrm{H} \to \mathrm{ZZ}^*/\mathrm{ZZ} \to \ell^+\ell^-\ell'^+\ell'^-$ channel.

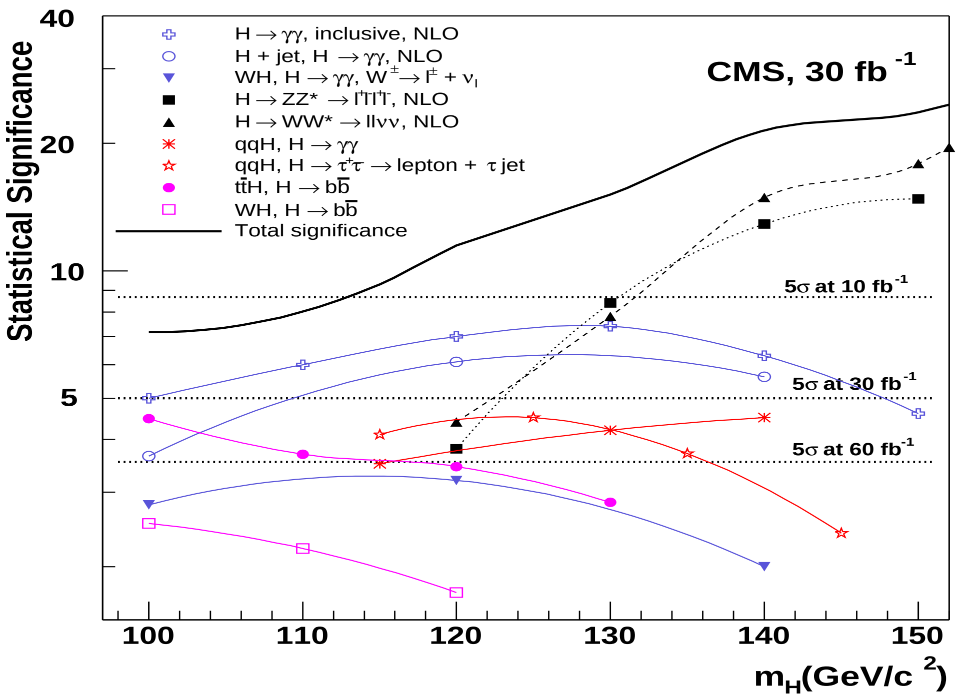

Figure 13: Expected statistical significance with 30 fb^{-1} for the SM Higgs boson as a function of $\mathrm{m_H}$ for $\mathrm{m_H} < 150$ GeV/c^2. The NLO cross sections for both signal and background were used for the inclusive $\mathrm{H} \to \gamma\gamma$, for $\mathrm{H}+$jet with $\mathrm{H} \to \gamma\gamma$ and for $\mathrm{H} \to \mathrm{ZZ}^* \to \ell^+\ell^-\ell'^+\ell'^-$ and $\mathrm{H} \to \mathrm{WW}^* \to \ell\ell\nu_\ell\nu_\ell$. Poisson statistics were used to calculate the statistical significance for the $\mathrm{H} \to \mathrm{ZZ}^* \to \ell^+\ell^-\ell'^+\ell'^-$, $\mathrm{H} \to \gamma\gamma$ in the WH production and $\mathrm{H} \to \gamma\gamma$ and $\mathrm{H} \to \tau^+\tau^-$ channels in the $\mathrm{qq} \to \mathrm{qqH}$ production.

4.2 Searches for heavy neutral MSSM Higgs bosons

The $\mathrm{H,A} \to \mu^+\mu^-$ decay channel in the $\mathrm{gg} \to \mathrm{b\bar{b}H/A}$ production was studied in Ref. [68] with full simulation and complete reconstruction. Figure 14 shows the reconstructed $\mu^+\mu^-$ invariant mass distribution of the $\mathrm{pp} \to \mathrm{b\bar{b}H/A{+}X}$, $\mathrm{H/A} \to \mu^+\mu^-$ signal, the Z,γ^* background and the $\mathrm{t\bar{t}}$ background with $\mathrm{m_A}$ = 130 GeV/c^2, tanβ = 30 for 20 fb^{-1}. The signal is a superposition of the A and H decays. The two-muon mass resolution of 1% is not good enough to resolve the 2 GeV/c^2 difference between the A and H boson masses in this parameter space point. Recent calculations show however that this mass difference could be as large as 5.5 GeV/c^2 for tan$\beta \sim$ 30 [69]. The dominant $\mathrm{Z},\gamma^* \to \mu^+\mu^-$ background was suppressed with b tagging. In the $\mathrm{gg} \to \mathrm{b\bar{b}H/A}$ production process b jets are soft ($\mathrm{E_T} \lesssim$ 50 GeV) and distributed over a wide rapidity range. An algorithm combining the secondary vertex and impact parameter tagging methods without a requirement of a reconstructed calorimeter jet was used to obtain a better signal efficiency ($\sim$ 40%) than that with a b-jet-tagging method. Because this b tagging technique does not require a jet to be reconstructed in the calorimeter the $\mathrm{t\bar{t}}$ background was suppressed efficiently by vetoing central jets.

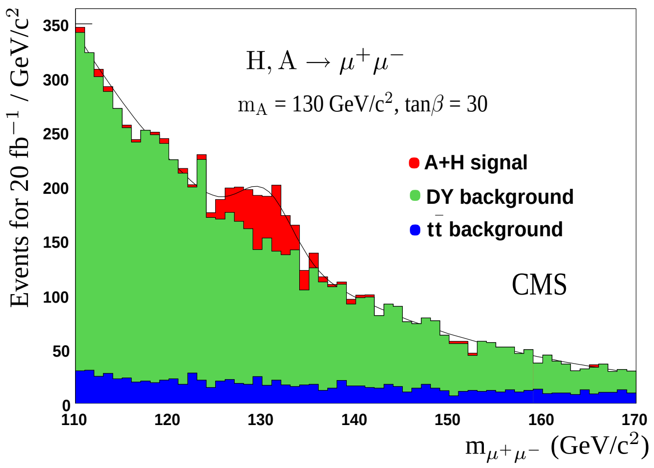

Figure 14: Reconstructed di-muon invariant mass distribution of the $\mathrm{pp} \to \mathrm{b\bar{b}H/A + X}$, $\mathrm{H/A} \to \mu^+\mu^-$ signal (dark), the Z,γ^* background (light) and the $\mathrm{t\bar{t}}$ background (black) with $\mathrm{m_H}$ = 130 GeV/c^2, tanβ = 30 for 20 fb^{-1}.

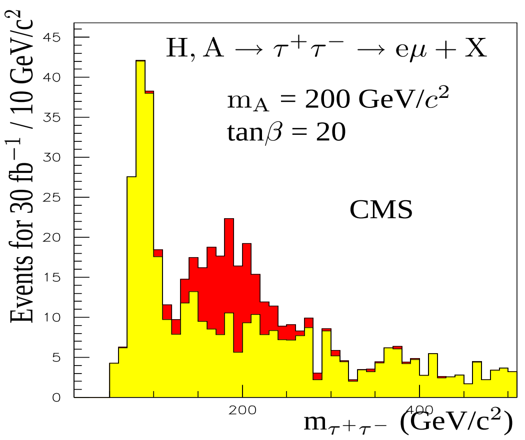

Figure 15: Reconstructed $\tau\tau$ invariant mass distribution in the $\mathrm{e}\mu$ final state in the $\mathrm{pp} \to \mathrm{b\bar{b}H/A + X}$, $\mathrm{H/A} \to \tau^+\tau^-$ signal (dark) and in the background (light) with $\mathrm{m_A}$ = 200 GeV/c^2 and tanβ = 20 for 30 fb^{-1}.

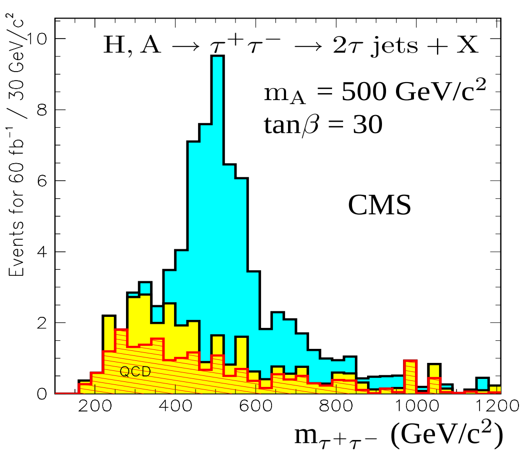

Figure 16: Reconstructed $\tau^+\tau^-$ invariant mass distribution in the two-τ-jet final state in the $\mathrm{pp} \to \mathrm{b\bar{b}H/A + X}$, $\mathrm{H/A} \to \tau^+\tau^-$ signal (dark), the total background (light) and in the QCD multi-jet background (dashed) with $\mathrm{m_A}$ = 500 GeV/c^2 and tanβ = 30 for 60 fb^{-1}.

The $e\mu$, $\ell^+\ell^-$ [47], lepton-plus-τ-jet [46] and two-τ-jet final states [14] were studied for the $H, A \rightarrow \tau^+\tau^-$ decay modes. Figure 15 shows the reconstructed $\tau^+\tau^-$ invariant mass distribution in the $e\mu$ final state in the $pp \rightarrow b\bar{b}H/A + X$, $H/A \rightarrow \tau^+\tau^-$ signal (dark) and in the background (light) with m_A = 200 GeV/c^2, tanβ = 20 for 30 fb^{-1}. A similar distribution is shown in Fig. 16 for the two-τ-jet final state in the $pp \rightarrow b\bar{b}H/A + X$, $H/A \rightarrow \tau^+\tau^-$ signal (dark), in the total background (light) and in the QCD multi-jet background (dashed) with m_A = 500 GeV/c^2, tanβ = 30 for 60 fb^{-1}. The identification of the hadronic τ decays for the two-τ-jet final state was performed with full simulation including the Level-1 trigger and HLT simulations [14]. For the suppression of the $Z, \gamma^* \rightarrow \tau^+\tau^-$ background and for further suppression the QCD multi-jet background, one associated b jet was reconstructed and tagged with the impact parameter method. For a background rejection factor of 100, the overall b-jet tagging efficiencies were found to be $\sim$ 20% due to the small E_T scale of the associated b jets and due to the importance of the forward tracking regions in the impact parameter measurements. The τ tagging with impact parameter measurement was also used to suppress the $Z \rightarrow \ell^+\ell^-$ background in the two-lepton final state and to further suppress the QCD multi-jet background in the two-τ-jet final state. The $t\bar{t}$ and Wt backgrounds with genuine b's and τ's from the $W \rightarrow \tau\nu_\tau$ decays were suppressed with a veto on a second central jet.

The uncertainty of the tanβ measurement from the event rates in the $H, A \rightarrow \tau^+\tau^-$ channels was found to be 17.2% for the two-τ-jet final state, 10.8% for the lepton-plus-τ-jet final state and 12.7% for the two-lepton final state for m_A = 200 GeV/c^2, tanβ = 20 with 30 fb^{-1} assuming a 20% theoretical uncertainty [7] and a 5% uncertainty in the luminosity measurement.

4.3 Searches for charged Higgs bosons.

Searches for the charged Higgs bosons in $t\bar{t}$ events ($m_{H^\pm} < m_{top}$) were studied in Ref. [70]. A lepton from one of the top quarks and hadronic τ decays from the $H^\pm \rightarrow \tau\nu_\tau$ decay channel are required. As the Higgs boson mass cannot be reconstructed in this channel the signal was obtained as an excess of τ's in the $t\bar{t}$ events relative to electrons and muons.

For the heavier charged Higgs bosons ($m_{H^\pm} > m_{top}$), the $H^\pm \rightarrow \tau\nu_\tau$ and $H^\pm \rightarrow tb$ decay channels were studied in associated production $gb \rightarrow tH^\pm$. To suppress the $t\bar{t}$ and Wt backgrounds with genuine τ's (for the $H^\pm \rightarrow \tau\nu_\tau$ decay channels with hadronic τ decays), the helicity correlations were exploited requiring at least 80% of the visible τ-jet energy to be carried by a single charged pion. Figure 17 shows the transverse mass reconstructed from the τ jet and E_T^{miss} in the $gg \rightarrow tH^\pm$, $H^\pm \rightarrow \tau\nu_\tau$, $\tau \rightarrow hadrons + \nu_\tau$ signal and in the background with $m_{H^\pm}$ = 200 GeV/c^2 and tanβ = 30 for 30 fb^{-1} [71]. In these purely hadronic events the E_T^{miss} originates mainly from the $H^\pm \rightarrow \tau\nu_\tau$ decay (for large $E_T^{\tau\ jet}$ cut) yielding an endpoint in the transverse mass at $m_{H^\pm}$ for the signal and at m_W for the residual backgrounds. These backgrounds can be further suppressed with a cut on the relative azimuthal angle $\Delta\varphi$ between the τ jet and the E_T^{miss} direction ($\Delta\varphi > 20°$ in Fig. 17). Figure 18 shows the

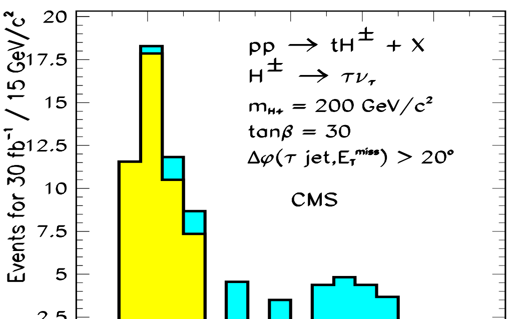

Figure 17: Transverse mass reconstructed from the τ jet and E_T^{miss} in the $gg \rightarrow tH^\pm$, $H^\pm \rightarrow \tau\nu_\tau$ signal (dark) and in the background (light) with $m_{H^\pm}$ = 200 GeV/c^2 and tanβ = 30 for 30 fb^{-1}.

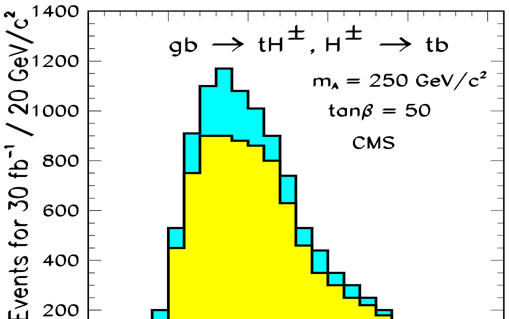

Figure 18: Invariant mass reconstructed from a b jet and jets from $t \rightarrow bq\bar{q}$ in the $gb \rightarrow tH^\pm$, $H^\pm \rightarrow tb$ signal (dark) and the background (light) with m_A = 250 GeV/c^2 and tanβ = 50 for 30 fb^{-1}.

invariant mass reconstructed from a b jet and jets from the $t \to bq\overline{q}$ decay in the $gb \to tH^{\pm}$, $H^{\pm} \to tb$ signal and the background with m_A = 250 GeV/c^2 and tanβ = 50 for 30 fb^{-1} [72]. To suppress the backgrounds from the $t\overline{t}$-plus-jet production (containing the irreducible $t\overline{t}b\overline{b}$ component) one leptonic and one hadronic top quark was reconstructed. The Higgs boson mass is given by one of the top quarks and one b-tagged jet leading to a large combinatorial background. Heavy charged Higgs bosons are accessible at large tanβ also in the s-channel production $q\overline{q} \to H^{\pm} \to \tau\nu_\tau$ with hadronic τ decays as was shown in Ref. [8]. The helicity correlations and transverse mass reconstruction were used to suppress the large $q\overline{q} \to W \to \tau\nu_\tau$ background.

The statistical uncertainty of the Higgs boson mass measurement from the transverse mass distributions for 30 fb^{-1} was found to be $\lesssim$ 2% in the $gb \to tH^{\pm}$, $H^{\pm} \to \tau\nu_\tau$ channel with tan$\beta > 30$ and $m_{H^{\pm}}$ = 400 GeV/c^2 and $\lesssim$ 15% in the $q\overline{q} \to H^{\pm} \to \tau\nu_\tau$ channel with tan$\beta > 20$ and $m_{H^{\pm}}$ = 200 GeV/c^2. The uncertainty of the tanβ measurement from the event rates in the $gb \to tH^{\pm}$, $H^{\pm} \to \tau\nu_\tau$ process for 30 fb^{-1} was found to be 14% with tanβ = 30 and $m_{H^{\pm}}$ = 200 GeV/c^2 and 20% with $m_{H^{\pm}}$ = 400 GeV/c^2 assuming a 20% theoretical uncertainty [7] and a 5% uncertainty in the luminosity measurement. In the $q\overline{q} \to H^{\pm} \to \tau\nu_\tau$ channel the tanβ uncertainty was found to be $\lesssim$ 15% with tan$\beta > 20$ and $m_{H^{\pm}}$ = 200 GeV/c^2 for 30 fb^{-1} [8].

4.4 Discovery potential in the MSSM

Figures 19 and 20 show the discovery potential for the lighter scalar MSSM Higgs boson h as a function of m_A and tanβ, assuming maximal stop mixing, m_{top} = 175 GeV/c^2 and m_{SUSY} = 1 TeV/c^2 for 30 and 100 fb^{-1}, respectively. The decay channels included in these figures are the inclusive $h \to \gamma\gamma$, $h \to ZZ^* \to \ell^+\ell^-\ell'^+\ell'^-$, $h \to \gamma\gamma$ in the associated production Wh, $h \to b\overline{b}$ in the associated production and $t\overline{t}h$, $h \to \gamma\gamma$ and $h \to \tau^+\tau^- \to \ell + \tau$ jet in the gauge boson fusion $qq \to qqh$. The NLO cross sections were used for the inclusive $h \to \gamma\gamma$ and $h \to ZZ^* \to \ell^+\ell^-\ell'^+\ell'^-$ channels. The $t\overline{t}h$,$h \to b\overline{b}$ channel covers the region $m_A \gtrsim$ 150 GeV/c^2 and tan$\beta \gtrsim$ 10 for 60 fb^{-1}. A region at large m_A and tanβ is not accessible with this channel due to the decreasing $h \to b\overline{b}$ branching fraction with increasing m_h. For the same reason the sensitivity in this channel is larger in the no-stop-mixing scenario. As the branching fraction for the $h \to ZZ^*$ decay decreases fast with decreasing m_h, the discovery potential for the $h \to ZZ^* \to \ell^+\ell^-\ell'^+\ell'^-$ channel is particularly sensitive to the MSSM parameters (mainly to the amount of stop mixing) through the maximum value of m_h ($\sim$ 127 GeV/c^2 for maximal stop mixing). For the MSSM scenarios where $m_h^{max} \lesssim$ 120 GeV/c^2 no sensitivity is expected in this channel. For the $h \to \tau^+\tau^-$ decay channel in the gauge boson fusion the region tan$\beta \gtrsim$ 4 is accessible for $m_A \gtrsim$ 150 GeV/c^2 apart from a small region with tan$\beta \gtrsim$ 20, $m_A \gtrsim$ 400 GeV/c^2 which requires higher integrated luminosity. For 60 fb^{-1}, the $h \to \gamma\gamma$ decay channel in the $qq \to qqh$ production covers the region $m_A \gtrsim$ 400 GeV/c^2 . The parameter space for 90 $\lesssim m_A \lesssim$ 130 GeV/c^2, where the lighter scalar is no more SM-like, is out of reach of the channels discussed in this Section. Investigations are in progress to cover this region with the $h \to \mu^+\mu^-$ and $h \to \tau^+\tau^-$ decay channels in the associated production $gg \to b\overline{b}h$, taking advantage of the b- and τ-tagging methods and mass reconstruction from τ's.

Figure 21 shows the 5σ-discovery potential for the heavy neutral MSSM Higgs bosons H and A in the $H, A \to \tau^+\tau^-$ and $H, A \to \mu^+\mu^-$ decay channels as a function of m_A and tanβ. The discovery potential for the two-lepton and lepton-plus-τ-jet final states from the $H, A \to \tau^+\tau^-$ decay channel are shown for 30 fb^{-1} while those for the two-τ-jet final states and for the $H, A \to \mu^+\mu^-$ channel are shown for 60 fb^{-1}. For the two-lepton final states with $m_A \lesssim$ 200 GeV/c^2, the $e\mu$ component yields a higher sensitivity than the $\ell\ell$ final state, which is overwhelmed with the direct $Z \to \ell^+\ell^-$ background near the Z peak, reducible only with τ tagging. Therefore the e^+e^- and $\mu^+\mu^-$ final states were ignored for $m_A \lesssim$ 200 GeV/c^2. The effect of the variation of the μ parameter on the discovery potential for the $H \to \tau^+\tau^- \to$ two τ-jet channel is also shown in Fig. 21.

Figure 22 shows the 5σ-discovery potential for the charged Higgs bosons as a function of m_A and tanβ for the $H^{\pm} \to \tau\nu_\tau$ decay channel with hadronic τ decays in the associated production $gb \to tH^{\pm}$, in the $t\overline{t}$ events and in the direct production $q\overline{q} \to H^{\pm}$. The potential is shown for maximal stop mixing and for an integrated luminosity of 30 fb^{-1}. The region around the top quark mass (140 GeV/c^2 $\lesssim m_A \lesssim$ 200 GeV/c^2) is still under investigation. The $gg \to tbH^{\pm}$ production process can be used with the $H^{\pm} \to \tau\nu_\tau$ decay mode.

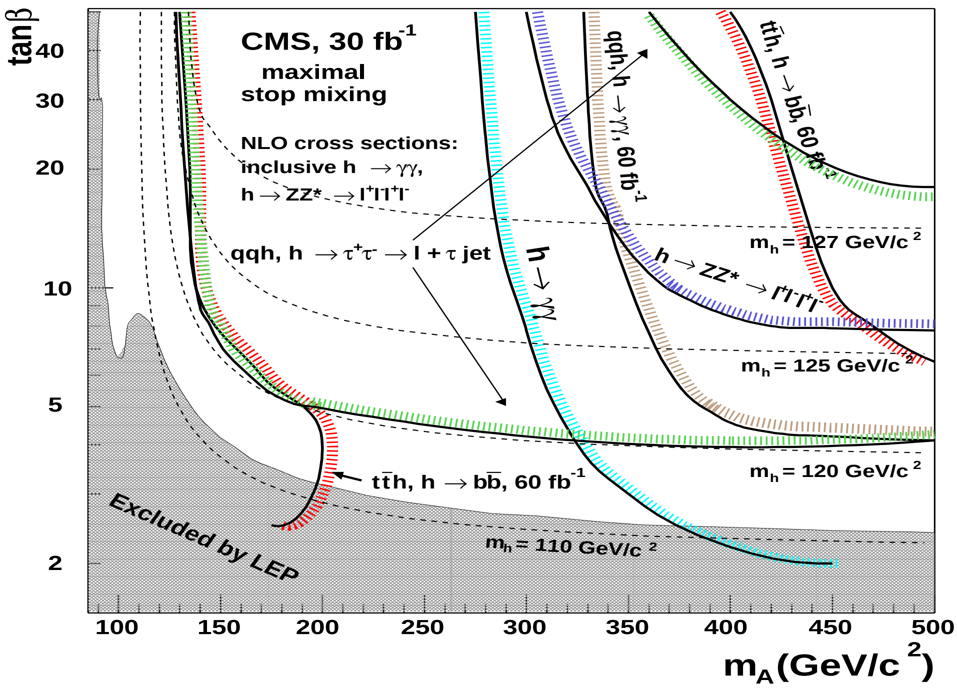

Figure 19: The 5σ-discovery potential for the lighter scalar MSSM Higgs boson as a function of $\mathrm{m_A}$ and tanβ for 30 fb^{-1} with maximal stop mixing. The potential for the $\mathrm{t\bar{t}h}$, $\mathrm{h} \to \mathrm{b\bar{b}}$ channel and for the $\mathrm{h} \to \gamma\gamma$ channel in the $\mathrm{qq} \to \mathrm{qqh}$ process are shown for 60 fb^{-1}. Poisson statistics were used to calculate the statistical significance for the $\mathrm{h} \to \mathrm{ZZ}^* \to \ell^+\ell^-\ell'^+\ell'^-$ channel and for the $\mathrm{h} \to \gamma\gamma$ and $\mathrm{h} \to \tau^+\tau^-$ decay channels in the $\mathrm{qq} \to \mathrm{qqh}$ production.

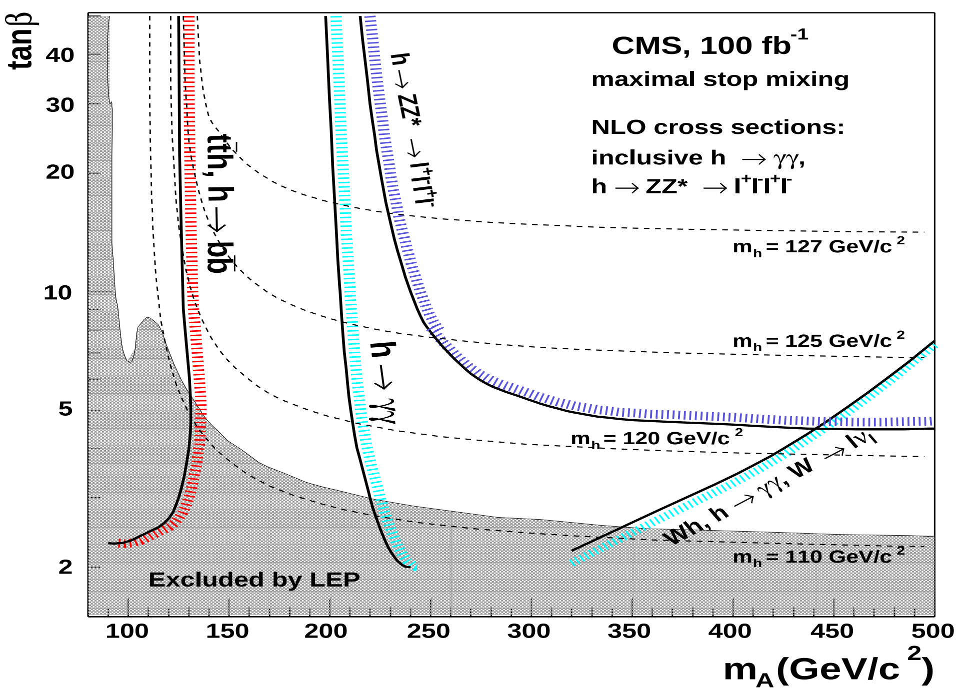

Figure 20: The 5σ-discovery potential for the lighter scalar MSSM Higgs boson as a function of $\mathrm{m_A}$ and tanβ for 100 fb^{-1} with maximal stop mixing. Poisson statistics were used to calculate the statistical significance for the $\mathrm{h} \to \mathrm{ZZ}^* \to \ell^+\ell^-\ell'^+\ell'^-$ channel and for the $\mathrm{h} \to \gamma\gamma$ decay channel in the Wh production.

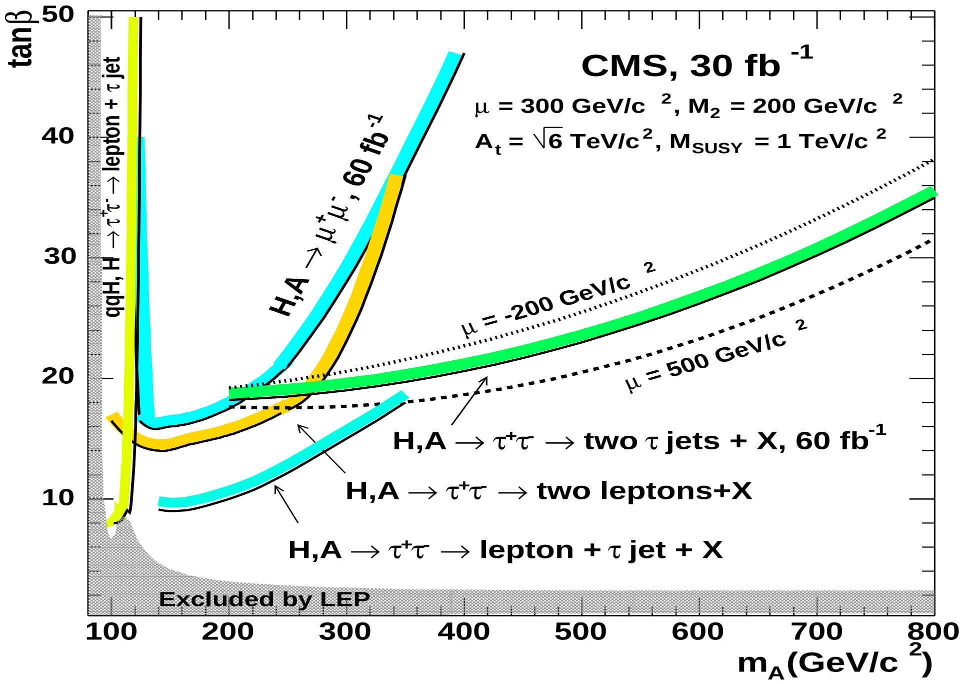

Figure 21: The 5σ-discovery potential for the heavy neutral MSSM Higgs bosons H and A with maximal stop mixing. Poisson statistics were used to calculate the statistical significance for the $\mathrm{H} \to \tau^+\tau^-$ channels in the $\mathrm{qq} \to \mathrm{qqH}$ production.

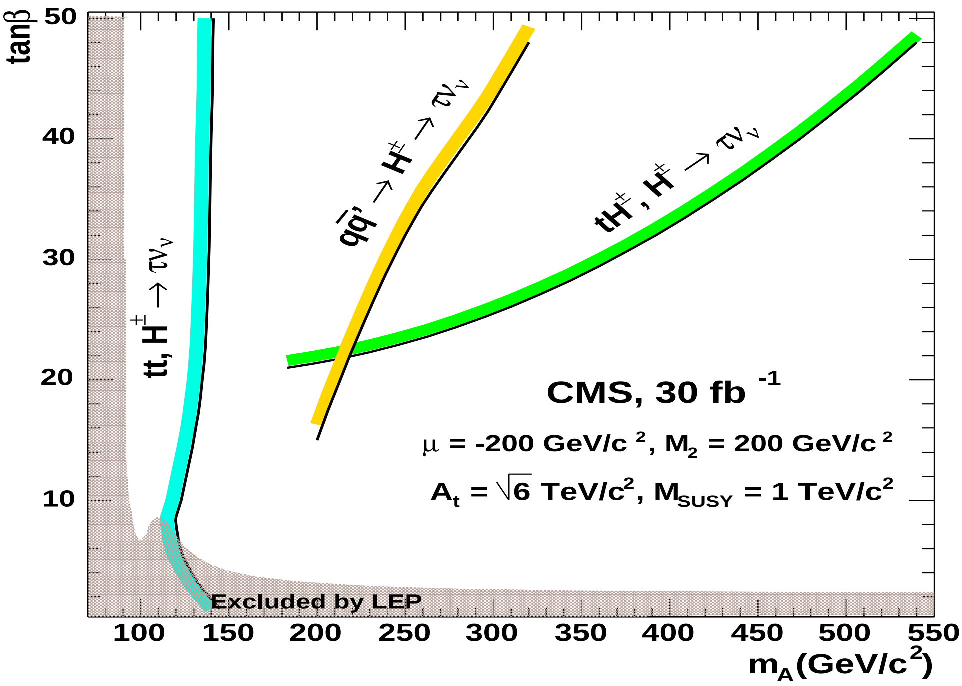

Figure 22: The 5σ-discovery potential for the charged Higgs bosons in the $\mathrm{gb} \to \mathrm{tH}^\pm$ and $\mathrm{t\bar{t}}$ production processes as a function of $\mathrm{m_A}$ and tanβ with 30 fb^{-1}. Poisson statistics were used to calculate the statistical significance for the $\mathrm{H}^\pm \to \tau\nu_\tau$ decay channel in the $\mathrm{gb} \to \mathrm{tH}^\pm$ production.

5 Specific SUSY searches

5.1 Higgs boson decays into gauginos

The four-lepton final state from the $\mathrm{H, A} \to \chi_2\chi_2$ decay channel with $\chi_2 \to \chi_1\ell^+\ell^-$ was studied in Ref. [73]. Figure 23 shows the four-lepton invariant mass distribution of the $\mathrm{H, A} \to \chi_2\chi_2$ signal and the background with $\mathrm{m_A}$ = 350 GeV/c^2, tanβ = 5, $\mathrm{M_2}$ = 120 GeV/c^2, μ = – 500 GeV/c^2, $\mathrm{M}_{\tilde{\mathrm{q}},\tilde{\mathrm{g}}}$ = 1000 GeV/c^2 and $\mathrm{M}_{\tilde{\ell}}$ = 250 GeV/c^2 for 100 fb^{-1} [73]. Lepton isolation, $\mathrm{E_T^{miss}}$ lower cut and jet veto were used to suppress the SM (ZZ, Zb$\bar{\mathrm{b}}$, Zc$\bar{\mathrm{c}}$, t$\bar{\mathrm{t}}$) and the sparticle ($\tilde{\mathrm{q}}$, $\tilde{\mathrm{g}}$) production backgrounds. Observation of the four-lepton signal in this channel requires understanding of origin, magnitude and shape of the various SM and SUSY backgrounds as the four-lepton invariant mass spectrum does not exhibit any kinematically obvious features. Examples of the 5σ-discovery reach for this channel are shown in Fig. 24.

For the charged Higgs bosons, the $\mathrm{gb} \to \mathrm{tH^\pm}$, $\mathrm{H^\pm} \to \chi_{2,3}\chi^\pm_{1,2}$ channel was studied in Ref. [74] in the three-lepton final state ($\chi_2 \to \chi_1\ell^+\ell^-$ and $\chi^\pm \to \chi_1\ell^\pm\nu_\ell$). To suppress the SM (t$\bar{\mathrm{t}}$, t$\bar{\mathrm{t}}$Z/$\gamma^*$, t$\bar{\mathrm{t}}$h) and SUSY backgrounds, a hadronically decaying associated top quark was reconstructed. This channel was found to be accessible only for

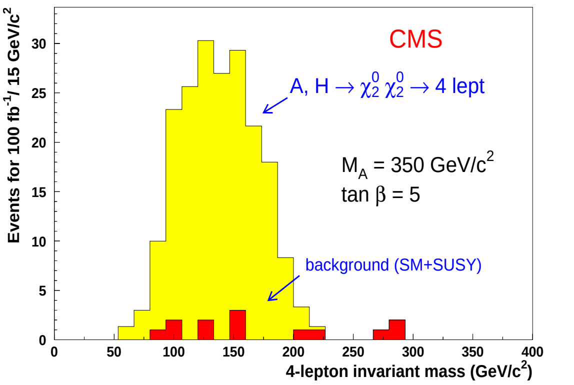

Figure 23: Invariant mass distribution reconstructed from four leptons of the $\mathrm{H, A} \to \chi_2\chi_2 \to \ell^+\ell^-\ell'^+\ell'^- + \mathrm{X}$ signal (light) and the SM+SUSY background (dark) with $\mathrm{m_A}$ = 350 GeV/c^2, tanβ = 5 for 100 fb^{-1}.

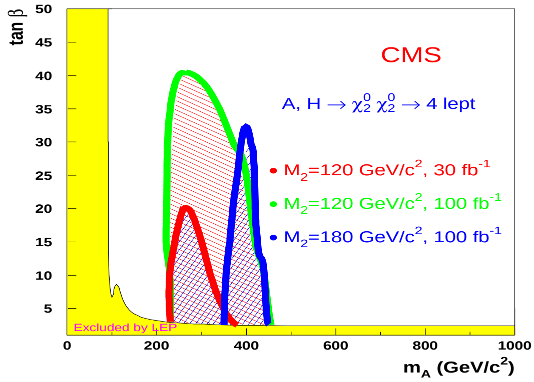

Figure 24: The 5σ-discovery potential for the $\mathrm{H, A} \to \chi_2\chi_2 \to \ell^+\ell^-\ell'^+\ell'^- + \mathrm{X}$ channel with $\mathrm{M_2}$ = 120 and 180 GeV/c^2 for 30 and 100 fb^{-1}.

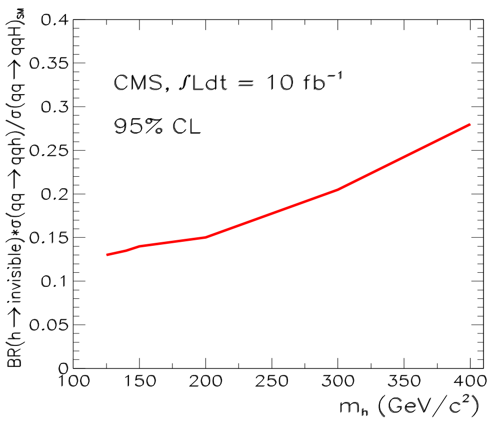

Figure 25: Expected 95% CL upper limit on the $\mathrm{h} \to$ invisible cross section normalized on SM cross section as a function of $\mathrm{m_H}$ for 10 fb^{-1}.

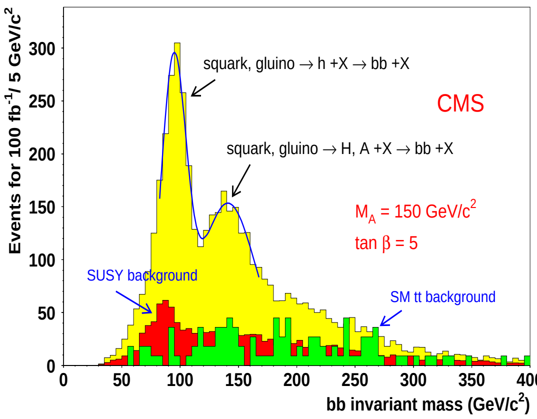

Figure 26: Invariant mass reconstructed from two b jets in the $\chi_2 \to \mathrm{h, H, A} + \chi_1$, $\mathrm{h, H, A} \to \mathrm{b\bar{b}}$ signal (light) and the SUSY (dark) and SM (gray) background with $\mathrm{m_A}$ = 150 GeV/c^2, tanβ = 5 for 100 fb^{-1}.

a limited fraction of the parameter space, namely for light sleptons and for $|\mu| \lesssim$ 150 GeV/c^2, i.e. near the LEP lower limit [74].

The invisible final states from the $\mathrm{h} \rightarrow \chi_1\chi_1$ decay channel in the $\mathrm{qq} \rightarrow \mathrm{qqh}$ production process were studied in Ref. [75]. Besides the backgrounds for which the $\mathrm{E_T^{miss}}$ originates from W and Z decays (electroweak or QCD production of Zjj and Wjj) there is a large potential background from QCD multi-jet events with the $\mathrm{E_T^{miss}}$ originating from measurement fluctuations or from heavy flavour decays. This multi-jet background can be suppressed with an upper limit on the angle $\Delta\varphi$ between the two tagging jets. For the QCD multi-jet background, these jets tend to be in a back-to-back configuration, with $\mathrm{E_T^{miss}}$ following one of the jets, whilst for the $\mathrm{qq} \rightarrow \mathrm{qqh}$ production the tagging jets tend to recoil against the $\mathrm{E_T^{miss}}$ from the $\mathrm{h} \rightarrow \chi_1\chi_1$ decay. The background levels can ultimately be obtained with a systematic uncertainty of $\sim$ 3% from the data themselves, taking advantage of Wjj and Zjj events with leptons reconstructed in $\mathrm{Z} \rightarrow \ell\ell$ and $\mathrm{W} \rightarrow \ell\nu_\ell$ decays [76]. Figure 25 shows the model independent 95% CL sensitivity to the $\mathrm{h} \rightarrow \mathrm{invisible}$ signal for 10 fb^{-1}. In the MSSM no sensitivity is expected in this channel for the heavy scalar H due to the suppression of the $\mathrm{qq} \rightarrow \mathrm{qqH}$ cross section while sensitivity in a major part of the parameter space can be expected for the lighter scalar Higgs boson h due to its SM like production.

5.2 Higgs bosons from the decays of gauginos

The production of h, H, A and $\mathrm{H}^{\pm}$ from gaugino decays in the MSSM was studied in Ref. [77]. Figure 26 shows the distribution of the reconstructed invariant $\mathrm{b\bar{b}}$ mass of the $\chi_2 \rightarrow \mathrm{h,H,A} + \chi_1$, $\mathrm{h,H,A} \rightarrow \mathrm{b\bar{b}}$ signal and the SUSY and SM background with $\mathrm{m_A}$ = 150 GeV/c^2, tanβ = 5, $\mathrm{M_2}$ = 350 GeV/c^2, μ = 1000 GeV/c^2, $\mathrm{m_{\tilde{g}}}$ = 1200 GeV/c^2, $\mathrm{m_{\tilde{q}}}$ = 800 GeV/c^2 and $\mathrm{m_{\tilde{\ell}}}$ = 500 GeV/c^2 for 100 fb^{-1}. For these parameter values, the Higgs bosons are produced mainly through the $\chi_2 \rightarrow \mathrm{h,H,A} + \chi_1$ and $\chi_1^{\pm} \rightarrow \mathrm{H}^{\pm}\chi_1$ decays. The residual $\mathrm{t\bar{t}}$ background is also shown in the figure. All neutral Higgs boson signals clearly emerge over the background in this part of parameter space. For larger values of $\mathrm{M_2}$ the rate decreases due to the suppression of the $\tilde{\mathrm{q}} \rightarrow \chi_2\mathrm{q}$, $\chi_1^{\pm}\mathrm{q}'$ transitions and the damping of the production cross section with increasing gluino mass. The discovery potential for the A and H

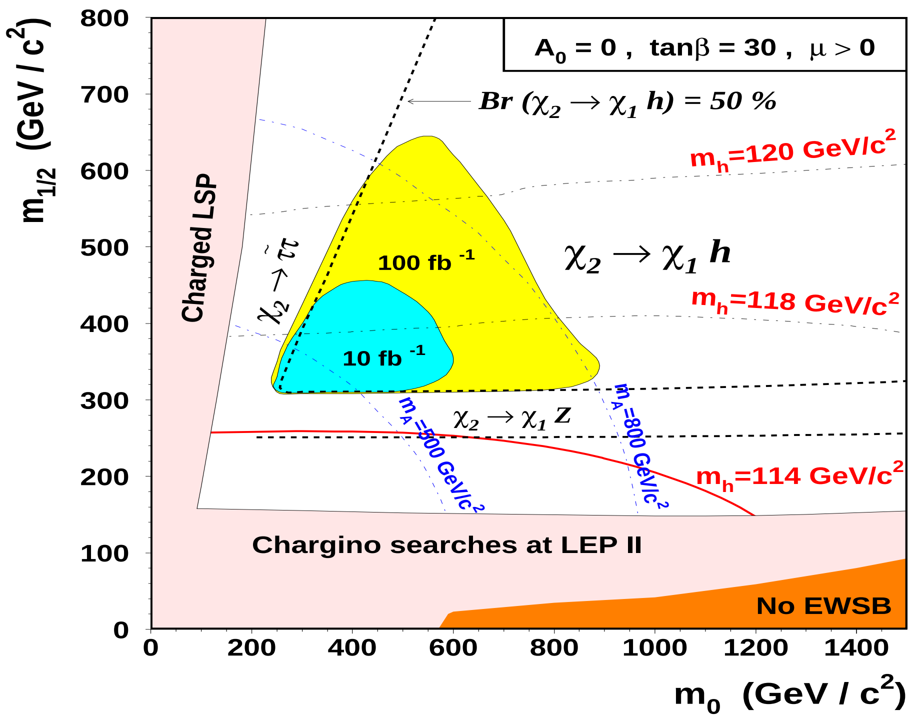

Figure 27: The 5σ-discovery potential for $\mathrm{h} \rightarrow \mathrm{b\bar{b}}$ from $\chi_2 \rightarrow \mathrm{h}\chi_1$ in the squark and gluino cascades with $\mathrm{A_0}$ = 0, tanβ = 30 and $\mu > 0$ for 10 and 100 fb^{-1}. The regions excluded in theory and by LEP searches are also shown in the figure.

bosons covers the region $m_A \lesssim$ 200 GeV/c^2 and is independent of tanβ, which makes these channels particularly interesting to cover the range 5 $\lesssim$ tan$\beta \lesssim$ 10.

The observability of the lighter scalar Higgs boson h in the SUSY cascades was studied in the mSUGRA framework [78]. Figure 27 shows the discovery potential for the $\chi_2 \to h\chi_1$, $h \to b\bar{b}$ channel in the squark and gluino cascades in the (m_0, $m_{1/2}$) plane with A_0 = 0, tanβ = 30 and $\mu > 0$ for 10 and 100 fb^{-1}. The regions excluded from theory and by LEP searches [79], isomass curves for the h and the A Higgs boson and the dominant decay modes are also shown in the figure. The 5σ-discovery potential, shown in Fig. 27 for mSUGRA, is valid also in the general MSSM if the mass spectrum is such that the $\tilde{g}/\tilde{q} \to \chi_2 \to \chi_1 h$ (or more generally $\tilde{g}/\tilde{q} \to \chi_i \to \chi_j h$) decays are allowed and the $\chi_i\chi_j h$ couplings are large enough.

6 Conclusions

The present understanding of the CMS potential for the SM and MSSM Higgs boson discovery has been presented. Some modifications can be expected as full simulation and reconstruction studies will continue in the coming years. The k factors for both signal and all relevant backgrounds will also be systematically investigated.

For the SM Higgs boson, a discovery is possible in the $H \to WW^*/WW$ and $H \to ZZ^*/ZZ$ decay channels in the mass range 130 GeV/$c^2 \lesssim m_H \lesssim$ 500 GeV/c^2 already with an integrated luminosity of 10 fb^{-1} or less and in the mass range 120 GeV/$c^2 \lesssim m_H \lesssim$ 1 TeV/c^2 with an integrated luminosity of 30 fb^{-1}. For $m_H \lesssim$ 130 GeV/c^2, the highest sensitivity (more than 5σ for 30 fb^{-1}) is obtained with the $H \to \gamma\gamma$ decay channel in the inclusive and in the H+jet production, while for $m_H >$ 130 GeV/c^2 the $H \to WW^*/WW$ and $H \to ZZ^*/ZZ$ decay channels dominate. The $H \to \gamma\gamma$ and $H \to \tau^+\tau^-$ decay channels are accessible in the gauge boson fusion production channels with $m_H \lesssim$ 150 GeV/c^2 for 60 fb^{-1}. For a 5σ statistical significance in the $H \to \gamma\gamma$ decay channel in the WH associated production even higher integrated luminosities are needed. The $H \to b\bar{b}$ channels yields its highest sensitivity around $m_H \sim$ 100 GeV/c^2. When all channels are combined, a 5σ statistical significance can be obtained for $m_H \geq$ 114 GeV/c^2 with an integrated luminosity of 10 fb^{-1}.

The lighter scalar MSSM Higgs boson is accessible through the inclusive $h \to \gamma\gamma$ ($m_A \gtrsim$ 200 GeV/c^2) and $h \to b\bar{b}$ ($m_A \gtrsim$ 130 GeV/c^2) decay channels with 100 fb^{-1}. The $h \to \tau^+\tau^-$ channel in the gauge boson fusion process leads to 5 σ significance for tan$\beta > 4$ and $m_A \gtrsim$ 150 GeV/c^2 already with an integrated luminosity of 30 fb^{-1}. The heavy neutral MSSM Higgs bosons are accessible through the $H, A \to \mu^+\mu^-$ and $H, A \to \tau^+\tau^-$ decays channels at large tanβ. The two-lepton and lepton-plus-τ-jet final states from the $H, A \to \tau^+\tau^-$ decays cover the domain $m_A \lesssim$ 300 GeV/c^2 and tan$\beta \gtrsim$ 10 already with 30 fb^{-1}. The two-τ-jet final states extend the sensitivity up to $m_A \sim$ 800 GeV/c^2 for tan$\beta \gtrsim$ 35 with 60 fb^{-1}. The heavy scalar H is accessible also in the $H \to \tau^+\tau^-$ channel in the gauge boson fusion for $m_A \lesssim$ 120 GeV/c^2 with 30 fb^{-1}. The heavy charged Higgs bosons can be searched for at large tanβ ($\gtrsim$ 20) with the $H^\pm \to \tau\nu_\tau$ decay channel in the associated production and in the direct production, and with the $H^\pm \to tb$ decay channel in the associated production. The $H^\pm \to \tau\nu_\tau$ decay channel in the associated production yields the highest sensitivity. The light charged Higgs bosons are accessible for $m_{H^\pm} \lesssim$ 140 GeV/c^2 through $t\bar{t}$ production. The intermediate and small tanβ range is accessible with the Higgs boson decays to neutralinos in the $H, A \to \chi_i\chi_j$ decay channel with 200 GeV/$c^2 \lesssim m_A \lesssim$ 450 GeV/c^2, $M_2 \leq$ 120 GeV/c^2 for 100 fb^{-1}. For the Higgs boson production from the gaugino decays in the $\tilde{g}$, $\tilde{q}$ cascades the region $m_A \lesssim$ 200 GeV/c^2 is accessible already with 30 fb^{-1}, independently of tanβ. For the tanβ measurement from event rates in the $gg \to b\bar{b}H/A$, $H, A \to \tau^+\tau^-$ channels, a precision better than 11% is expected from combination of the three final states for tan$\beta \geq$ 20 and m_A = 200 GeV/c^2 with 30 fb^{-1}. For the charged Higgs bosons in the $gb \to tH^\pm$, $H^\pm \to \tau\nu_\tau$ channel a precision better than 20% is expected within the 5σ-discovery domain with 30 fb^{-1}.

Acknowledgements

The authors would like to thank A. Djouadi, S. Moretti, T. Plehn, D. Rainwater, D.P. Roy, M. Spira and D. Zeppenfeld for helpful discussions. One of us (V.D.) would like to thank the European Community for financial support (fellowship HPRN-CT-2002-00326).

The authors are grateful to all members of the Editorial Board, P. Janot, I. Van Vulpen, N. Marinelli, N. Neumeister, D. Denegri and V. Hagopian.

References

[1] S. Heinemeyer and G. Weiglein, Leading Electroweak Two-Loop Corrections to Precision Observables in the MSSM, J. High Energy Phys. 10 (2002) 072.

[2] M. Carena, S. Heynemeyer, C.E.M. Wagner and G. Weiglein, Suggestions for improved benchmark scenarios for Higgs-boson searches at LEP2, CERN-TH/99-374, DESY 99-186, hep-ph/9912223.

[3] LEP Higgs Working Group, Phys. Lett. **B565** (2003) 61.

[4] LEP Higgs Working Group, Searches for the Neutral Higgs Bosons of the MSSM, hep-ex/0107030.

[5] The LEP Electroweak Working Group, http://lepewwg.web.cern.ch/LEPEWWG/.

[6] M. Spira, HIGLU, hep-ph/9510347; M. Spira, Fortsch. Phys. 46 (1998) 203.

[7] T. Plehn, Charged Higgs Boson Production in Bottom-Gluon Fusion, hep-ph/0206121; E. Boos and T. Plehn, Higgs Boson Production Induced by Bottom Quarks, hep-ph/0304034.

[8] S. Slabospitsky, Study of s-Channel Charged Higgs Production in CMS, CMS NOTE 2002/010, hep-ph/0203094.

[9] M. Carena, J.S. Conway, H.E. Haber and J. Hobbs, Report of the Higgs Working Group of the Tevatron Run 2 SUSY/Higgs Workshop, hep-ph/0010338 and references therein; S. Moretti and J. Rathsman, Pair production of charged Higgs bosons in association with bottom quark pairs at the Large Hadron Collider, hep-ph/0308215.

[10] R. Rainwater, M. Spira and D. Zeppenfeld, Higgs Boson Production at Hadron Colliders, hep-ph/0203187.

[11] A. Djouadi, J. Kalinowski and M. Spira, HDECAY: a program for Higgs Boson Decays in the Standard Model and its Supersymmetric Extension, hep-ph/9704448.

[12] D. Zeppenfeld, Int. J. Mod. Phys. **A16** (2001) 831; T. Plehn, D. Rainwater, D. Zeppenfeld, Phys. Rev. Lett. **88** (2002) 051801; Phys. Lett. **B454** (1999) 297., M.L. Mangano et. al., CERN-TH/2002-287.

[13] D.P. Roy, Phys. Lett. **B459** (1999) 607.

[14] R. Kinnunen and A. Nikitenko, Study of $\mathrm{H} \rightarrow \tau^+\tau^-$ with hadronic τ decays in CMS, CMS NOTE-2003/006.

[15] A. Djouadi, Phys. Lett. **B435** (1998) 101.

[16] R. Kinnunen, S. Lehti, A. Nikitenko and S. Rantala, Effects of large mixing and light stop for $\mathrm{h} \rightarrow \gamma\gamma$ in MSSM, CMS NOTE 2000/043.

[17] CMS Collaboration, The Magnet Project, Technical Design Report, CERN/LHCC 97-10, CMS TDR 1, 1997.

[18] CMS Collaboration, The Tracker Project, Technical Design Report, CERN/LHCC 98-6, CMS TDR 5, 1998.

[19] CMS Collaboration, CERN/LHCC 2000-016, CMS TDR 5 Addendum 1, 21 February 2000.

[20] CMS Collaboration, The Electromagnetic Calorimeter Project, Technical Design Report, CERN/LHCC 97-33, CMS TDR 4, 1997.

[21] CMS Collaboration, The Hadron Calorimeter Project, Technical Design Report, CERN/LHCC 97-31, CMS TDR 2, 1997.

[22] CMS Collaboration, The Muon Project, Technical Design Report, CERN/LHCC 97-32, CMS TDR 3, 1997.

[23] CMS Collaboration, CMS Simulation and Reconstruction Package, http://cmsdoc.cern.ch/cmsim/cmsim.html.

[24] S. Abdullin, A. Khanov and N. Stepanov, CMSJET, CMS TN/94-180.

[25] V. Drollinger, V. Karimaki, S. Lehti and N. Stepanov, private communication.

[26] CMS Collaboration, Trigger and Data Acquisition Systems, Technical Design Report, CERN/LHCC 2000-38, CMS TDR 6.1, 2000.

[27] CMS Collaboration, The Data Acquisition and High-Level Trigger Project, Technical Design Report, CERN/LHCC 2002-26, CMS TDR 6.2, 2002.

[28] K. Lassila-Perini, Discovery potential of the Standard Model Higgs in CMS at the LHC, Dissertation, ETH No. 12961 (1998).

[29] E. Meschi et al., Electron Reconstruction in the CMS Electromagnetic Calorimeter, CMS NOTE 2001/034.

[30] A. Nikitenko, P. Verrecchia, D. Bomestar, I. $\mathrm{Z} \rightarrow \mathrm{e^+e^-}$ and $\mathrm{H} \rightarrow 4\mathrm{e}^{\pm}$ Mass Reconstruction in $\mathrm{PbWO_4}$ Crystal ECAL with GEANT simulation of CMS detector; II. Electrons of $\mathrm{E_T}$ = 30 GeV at η=0.1 and 1.3 in CMS Detector : E/p Matching, Calibration, Resolution, CMS TN/95-019.

[31] I. Puljak, Potentiel de decouverte du boson de Higgs dans le canal $\mathrm{H} \rightarrow \mathrm{ZZ}^* \rightarrow 4\mathrm{e}^{\pm}$ avec le detecteur CMS. Contribution a la construction du calorimetre electromagnetique de CMS, Dissertation, Ecole Polytechnique, Palaiseau, France, 2000.

[32] W. Adam et al., Reconstruction of electrons with the Gaussian-sum filter in the CMS tracker at LHC, CMS CR 2003/012.

[33] I. Iashvili, R. Kinnunen, A. Nikitenko and D. Denegri, Study of the $\mathrm{H} \rightarrow \mathrm{ZZ}^* \rightarrow \ell^+\ell^-\ell'^+\ell'^-$ Channel in CMS, CMS TN/95-059 (1995); M. Dzelalija, Z. Antunovic and R. Kinnunen, Study of heavy $\mathrm{H} \rightarrow \mathrm{ZZ} \rightarrow \ell^+\ell^-\ell'^+\ell'^-$ in CMS, CMS TN/95-076.

[34] C. Charlot, A. Nikitenko, I. Puljak, I. Soric, Comparison of fixed window and clusterization algorithms for $\mathrm{Z} \rightarrow \mathrm{e^+e^-}$ and $\mathrm{H} \rightarrow 4\mathrm{e}^{\pm}$ mass reconstruction in CMS $\mathrm{PbWO_4}$ crystal ECAL for Higgs mass 170 and 130 GeV, CMS TN/95-101.

[35] D. Bomestar, D. Denegri, R. Kinnunen, A. Nikitenko, Study of H$\rightarrow$ $\mathrm{ZZ}^*/\mathrm{ZZ} \rightarrow 4\ell$ with a full GEANT simulation of CMS, CMS TN/95-018.

[36] J.E. Huth et al. in Proceeding of Research Directions For The Decade: Snowmass 1990, July 1990, edited by E.L. Berger (World Scientific, Singapore, 1992), p. 134.

[37] D. Green et al., Energy Flow Objects and Usage of Tracks for Energy Measurement in CMS, CMS NOTE 2002/036.

[38] O. Kodolova, I. Vardanyan, S. Kunori and A. Nikitenko, private communication.

[39] A. Nikitenko, S. Kunori and R. Kinnunen, Missing Transverse Energy Measurement with Jet Energy Corrections, CMS NOTE 2001/040.

[40] A. Nikitenko, J. Varela, A study of the 1st Level τ trigger, CMS TN/95-195.

[41] S. Eno, A. Nikitenko, R. Kinnunen, private communication.

[42] R. Kinnunen, A. Nikitenko, Study of τ jet identification in CMS, CMS NOTE 1997/002.

[43] S. Eno et al., A Study of a First and Second Level Tau Trigger, CMS NOTE 2000/055.

[44] D. Kotlinski, A. Nikitenko and R. Kinnunen, Study of a Level-3 Tau Trigger with the Pixel Detector, CMS NOTE 2001/017.

[45] G. Bagliesi, S. Gennai and G. Sguazzoni, A L2 Trigger for Tau Hadronic Decays with Tracker Isolation in the Low Luminosity Scenario, CMS NOTE 2002/018.

[46] R. Kinnunen and A. Nikitenko, Study of $\mathrm{H_{SUSYS}} \rightarrow \tau\tau \rightarrow \ell^{\pm} + \tau\ \mathrm{jet} + \mathrm{E_T^{miss}}$ in CMS, CMS NOTE 1997/106.

[47] S. Lehti, Prospects for the Detection of the MSSM Higgs Bosons Decaying into Tau Leptons in the CMS Detector, Dissertation, University of Helsinki, Report Series in Physics, HU-P-D93, 2001.

[48] G. Segneri, F. Palla, Lifetime based b tagging with CMS, CMS NOTE 2002 / 046

[49] T. Sjostrand et al., High-Energy Physics Event Generation with PYTHIA 6.1, Comput. Phys. Commun. **135** (2001) 238.

[50] G. Corcella et al., HERWIG 6: An event generator for hadron emission reactions with interfering gluons (including SUSY processes), JHEP 0101 (2001) 010.

[51] H. Baer, F.E. Paige, S.D. Protopopescu and X. Tata, hep-ph/0001086

[52] A. Pukhov et al. CompHEP - a package for evaluation of Feynman diagrams and integration over multi-particle phase space, INP-MSU 98-41/542.

[53] A.S.Belyaev et.al., CompHEP-PYTHIA interface, Proc.of VII int.workshop on advanced computing and analysis techniques in physics research (ACAT2000), Batavia, 2000, hep-ph/0101232.

[54] K. Hagiwara and D. Zeppenfeld, Nucl.Phys. $\mathbf{B313}$ (1989) 560

[55] S. Jadach et al., Comput. Phys. Commun. $\mathbf{76}$ (1993) 361.

[56] M. Dittmar and H. Dreiner, LHC Higgs Search with $\ell\nu\ell\overline{\nu}$ Final States, CMS NOTE-1997/083.

[57] D. Green et al., Search for the Standard Model Higgs Boson with $\mathrm{M_H} \simeq$ 170 GeV/c^2 in $\mathrm{W^+W^-}$ Decay Mode, CMS NOTE-1998/089, J.Phys.G.Nucl.Part.Phys. $\mathbf{26}$ (2000) 1751.

[58] M.N. Dubinin, V.A. Ilyin and V.I. Savrin, Light Higgs Boson Signal at LHC in the Reactions $\mathrm{pp} \rightarrow \gamma\gamma + \mathrm{jet}$ and $\mathrm{pp} \rightarrow \gamma\gamma + \mathrm{lepton}$, CMS NOTE 1997/101; S. Abdullin et al., Phys. Lett., $\mathbf{B431}$ (1998) 410.

[59] D. de Florian and Z. Kunszt, Phys.Lett. $\mathbf{B460}$ (1999) 184; C. Balazs, P. Nadolsky, C. Schmidt and C.P. Yuan, Phys.Lett. $\mathbf{B489}$ (2000) 157

[60] V. Drollinger, Th. Muller and D. Denegri, Searching for Higgs Bosons in Association with Top Quark Pairs in the $\mathrm{H} \rightarrow \mathrm{b\overline{b}}$ Decay Mode, CMS NOTE 2001/054, hep-ph/0111312; V. Drollinger, Th. Muller and D. Denegri, Prospects for Higgs Bosons Searches in the Channel $\mathrm{W^\pm H} \rightarrow \ell^\pm \nu \mathrm{b\overline{b}}$, CMS NOTE 2002/006, hep-ph/0201249.

[61] D. Green et al., A Study of $\mathrm{t\overline{t}} + \mathrm{H}$ at CMS, CMS NOTE-2001/039.

[62] D. Benedetti and L. Fano, Study of High Level b-trigger Selection of ttH Fully Hadronic Decays, CMS NOTE-2002/044.

[63] M. Dubinin, Higgs Boson Signal in the Reaction $\mathrm{pp} \rightarrow \gamma\gamma + \mathrm{two\ Forward\ Jets}$, CMS NOTE 2001/022.

[64] N. Akchurin et al., Study of Low Mass Higgs Using $\mathrm{pp} \rightarrow \mathrm{q\overline{q}H}$ at CMS, CMS NOTE-2002/016.

[65] G. Azuelos et al., Search for the SM Higgs boson using vector boson fusion at the LHC, Workshop on Physics at TeV Colliders, Les Houches, France, 2001, hep-ph/0203056.

[66] H.D. Yildiz, Observing Higgs in Weak Boson Fusion with Forward Jet Tagging at the CERN CMS Experiment, Diss. Middle East Technical University, Ankara, Turkey, 2002.

[67] H.D. Yildiz, M. Zeyrek and R. Kinnunen, Study of $\mathrm{pp} \rightarrow \mathrm{jjH}$ with $\mathrm{H} \rightarrow \mathrm{WW} \rightarrow \ell\nu\mathrm{q\overline{q}}$ in CMS for $\mathrm{m_H}$ = 300 and 600 GeV/c^2, CMS NOTE-2001/050.

[68] L. Bellucci, MSSM Neutral Higgs Boson searches at CMS in the $\mu^+\mu^-$ channel, Dissertation, Universita degli studi di Firenze, December, 2001.

[69] E. Boos, A. Djouadi and A. Nikitenko, Detection of the neutral MSSM Higgs bosons in the intense-coupling regime at the LHC, CERN TH/2003-152.

[70] S. Banerjee and M. Maity, Search for the Charged Higgs in Top Decays in CMS, CMS NOTE 2000/039.

[71] R. Kinnunen, Study of Heavy Charged Higgs in $\mathrm{pp} \rightarrow \mathrm{tH^\pm}$ with $\mathrm{H^\pm} \rightarrow \tau\nu_\tau$ in CMS, CMS NOTE 2000/045.

[72] P. Salmi, R. Kinnunen and N. Stepanov, Prospects of Detecting Massive Charged Higgs from Hadronic Decay $\mathrm{H^\pm} \rightarrow \mathrm{tb}$ in CMS, CMS NOTE-2002/024.

[73] S. Abdullin, D. Denegri and F. Moortgat, Observability of MSSM Higgs bosons via sparticle decay modes in CMS, CMS NOTE 2001/042.

[74] M. Bisset, F. Moortgat, S. Moretti, Trilepton+top signal from chargino-neutralino decays of MSSM charged Higgs bosons at the LHC, CMS NOTE 2003/004, hep-ph/0303093.

[75] B. Di Girolamo et al., Experimental Observation of an invisible Higgs Boson at LHC, Summary Report (2001), Workshop on Physics at TeV Colliders, Les Houches, France, 2001, hep-ph/0203056.

[76] O.J.P. Eboli and D. Zeppenfeld, Phys.Lett. **B495** (2000) 147.

[77] A. Datta, A. Djouadi, M. Guchait and F. Moortgat, Detection of MSSM Higgs bosons from SUSY particle cascade at the LHC, hep-ph/0303095.

[78] S. Abdullin and D. Denegri, On the Possibility to Observe $\mathrm{h} \rightarrow \mathrm{b\bar{b}}$ with S/B$\sim$1 in SUSY (mSUGRA), and Implications for Tracker and HCAL CMS NOTE-1997/070.

[79] OPAL Collaboration, Search for nearly mass degenerate Charginos and neutralinos at LEP, CERN-EP-2002-063, Submitted to Eur.Phys.J; ALEPH Collaboration, Search for charginos nearly mass degenerate with the lightest neutralino in $\mathrm{e^+e^-}$ collisions at centre-of-mass energies up to 209 GeV, Phys.Lett. **B533** (2002).